

Article

Boosted Photocatalytic Performance for Antibiotics Removal with Ag/PW₁₂/TiO₂ Composite: Degradation Pathways and Toxicity Assessment

Hongfei Shi ^{1,*} , Haoshen Wang ¹, Enji Zhang ¹, Xiaoshu Qu ¹ , Jianping Li ^{1,*}, Sisi Zhao ², Huajing Gao ¹ and Zhe Chen ¹

¹ Institute of Petrochemical Technology, Jilin Institute of Chemical Technology, Jilin City 132022, China; 18638813901@163.com (H.W.); 13664448948@163.com (E.Z.); xiaoshuqu@jlct.edu.cn (X.Q.); huajing_gao@163.com (H.G.); chenzhec999@163.com (Z.C.)

² Institute of Catalysis for Energy and Environment, College of Chemistry & Chemical Engineering, Shenyang Normal University, Shenyang 110034, China; zhaoss0905@163.com

* Correspondence: shihf813@nenu.edu.cn (H.S.); lij156@nenu.edu.cn (J.L.)

Abstract: Photocatalyst is the core of photocatalysis and directly determines photocatalytic performance. However, low quantum efficiency and low utilization of solar energy are important technical problems in the application of photocatalysis. In this work, a series of polyoxometalates (POMs) [H₃PW₁₂O₄₀] (PW₁₂)-doped titanium dioxide (TiO₂) nanofibers modified with various amount of silver (Ag) nanoparticles (NPs) were prepared by utilizing electrospinning/photoreduction strategy, and were labelled as *x* wt% Ag/PW₁₂/TiO₂ (*abbr.* *x*% Ag/PT, *x* = 5, 10, and 15, respectively). The as-prepared materials were characterized with a series of techniques and exhibited remarkable catalytic activities for visible-light degradation tetracycline (TC), enrofloxacin (ENR), and methyl orange (MO). Particularly, the 10% Ag/PT catalyst with a specific surface area of 155.09 m²/g and an average aperture of 4.61 nm possessed the optimal photodegradation performance, with efficiencies reaching 78.19% for TC, 93.65% for ENR, and 99.29% for MO, which were significantly higher than those of PW₁₂-free Ag/TiO₂ and PT nanofibers. Additionally, various parameters (the pH of the solution, catalyst usage, and TC concentration) influencing the degradation process were investigated in detail. The optimal conditions are as follows: catalyst usage: 20 mg; TC: 20 mL of 20 ppm; pH = 7. Furthermore, the photodegradation intermediates and pathways were demonstrated by HPLC-MS measurement. We also investigated the toxicity of products generated during TC removal by employing quantitative structure-activity relationship (QSAR) prediction through a toxicity estimation software tool (T.E.S.T. Version 5.1.2.). The mechanism study showed that the doping of PW₁₂ and the modification of Ag NPs on TiO₂ broadened the visible-light absorption, accelerating the effective separation of photogenerated carriers, therefore resulting in an enhanced photocatalytic performance. The research provided some new thoughts for exploiting efficient and durable photocatalysts for environmental remediation.

Keywords: Ag nanoparticles; PW₁₂/TiO₂ nanofibers; degradation of antibiotics; degradation pathways; toxicity assessment



Citation: Shi, H.; Wang, H.; Zhang, E.; Qu, X.; Li, J.; Zhao, S.; Gao, H.; Chen, Z. Boosted Photocatalytic Performance for Antibiotics Removal with Ag/PW₁₂/TiO₂ Composite: Degradation Pathways and Toxicity Assessment. *Molecules* **2023**, *28*, 6831. <https://doi.org/10.3390/molecules28196831>

Academic Editor: Sugang Meng

Received: 7 September 2023

Revised: 22 September 2023

Accepted: 25 September 2023

Published: 27 September 2023



Copyright: © 2023 by the authors. Licensee MDPI, Basel, Switzerland. This article is an open access article distributed under the terms and conditions of the Creative Commons Attribution (CC BY) license (<https://creativecommons.org/licenses/by/4.0/>).

1. Introduction

In recent years, photocatalysis technology, which can use solar energy for environmental purification and energy conversion, has received worldwide attention [1,2]. Photocatalytic technology has a wide range of applications in pollutants degradation, CO₂ reduction, water splitting to produce hydrogen and nitrogen fixation, etc. [3]. The core of photocatalysis is designing and developing the photocatalysts with visible-light response, prominent catalytic activity, and recyclability. Among the various photocatalysts, TiO₂ has received a lot of attention due to its low synthesis cost, lack of toxicity, and high catalytic

activity [4]. However, the wide band gap and low utilization efficiency of carriers limit its practical applications [5]. Therefore, it is urgent to enhance the visible-light absorption and the driving force for the separation of photoinduced carriers. Many strategies have been made to improve its catalytic activity, including dye sensitization [6], construction of heterojunction [7], morphology engineering [8], and metal/non-metal element doping, etc. [9].

POMs are identified as a promising candidate to embellish TiO_2 for addressing this challenge. POMs demonstrate semiconductor-like characteristics with their tunable electronic structures and energy levels. They also possess high negative charge and excellent solubility and are endowed with favorable processing properties [10,11]. Therefore, POMs are easily encapsulated or dispersed within various semiconductors, which can constantly enhance the redox property, modulate the band gap structure, and facilitate the separation efficiency of photoproduced carriers [12–14]. Among various POMs, $\text{H}_3\text{PW}_{12}\text{O}_{40}$ (abbr. PW_{12}), as a Keggin-type POM, has demonstrated important applications in photocatalysis fields such as water splitting and contaminants removal [15,16].

Besides, the strategy of noble metals (such as Ag, Pd, Pt, and Au) modifying semiconductors has been extensively investigated to expand spectral absorption and accelerate the separation of photon-generated carriers [17–19]. Typically, a Schottky junction is formed at the interface between a metal and a semiconductor to create a built-in electric region that enhances the surface plasmon resonance (SPR) effect. Among these noble metals, Ag has been extensively applied in SPR photocatalysis due to the excellent electrical conductivity, relatively cheap price, wide SPR absorption, and intense local electromagnetic fields caused by SPR [20,21]. For instance, Ag@TiO_2 composites with core-shell nanostructures were prepared, applying the one-step solvothermal method by Zeng et al., which displayed enhanced light absorption range and enabled the effective separation of e^- - h^+ pairs, resulting in an improved photocatalytic performance [22]. Moreover, the electrostatic spinning technology has been considered as a versatile technology capable of adjusting the composition, diameter, and orientation of materials according to the intended function and application [23], which is employed extensively in the fabrication of metal oxides (TiO_2 , ZnO , Fe_2O_3 , WO_3 , etc.) nanofibers for photocatalytic degradation of pollutants [24], hydrogen production [25], and CO_2 reduction [26], etc.

Based on the above considerations, we prepared a novel $\text{Ag}/\text{PW}_{12}/\text{TiO}_2$ (abbr. Ag/PT) composite by electrospinning/photoreduction methods, according to the literature [11,19]. Firstly, the electrospinning/calcination method was used to obtain $\text{PW}_{12}/\text{TiO}_2$ material; then, the Ag NPs were loaded on $\text{PW}_{12}/\text{TiO}_2$ using the photoreduction method, obtaining the Ag/PT composite. Moreover, these as-prepared Ag/PT nanofibers exhibited remarkable photocatalytic activities for the degradation of multiple pollutants. The 10% Ag/PT catalyst possessed the optimal photodegradation performance, whose efficiency reached 78.19% for TC, 93.65% for ENR, and 99.29% for MO, which was significantly higher than those of PW_{12} -free Ag/TiO_2 and PT. Furthermore, the influence parameters, including the pH of the solution, catalyst usage, and the concentration of TC, were studied in detail. The degradation intermediates and pathways were revealed by LC-MS data. QSAR prediction was employed to investigate the toxicity of products in TC photodegradation. Ultimately, the photocatalytic mechanism was investigated with radical capture analysis and band gap structures.

2. Results and Discussion

2.1. Characterization of Ag/PT Composites

The microstructure and morphology of PT nanofibers are presented in Figure 1a. The surface of the nanofibers after calcination at $550\text{ }^\circ\text{C}$ is relatively rough and porous, and the fiber diameter is about $80 \pm 20\text{ nm}$. Figure 1b,c show the SEM and TEM images for 10% Ag/PT , respectively. Distinctly, these Ag NPs are equally deposited on the surface of PT with an average diameter of $10 \pm 5\text{ nm}$. The HRTEM images of 10% Ag/PT verify the latticed coexistence of TiO_2 and Ag in these samples (Figure 1d). The observed lattice spacing of 0.233 nm corresponds to the (112) crystal plane of the anatase phase TiO_2 (JCPDS

no. 21-1272), and the lattice spacing of 0.145 nm corresponds to the Ag (220) plane (JCPDS no. 04-0783). As shown in Figure 1e–j, the elemental mapping images of 10% Ag/PT and the EDS data (Figure S1) further indicated the uniform distribution of Ag, P, W, Ti, and O elements in the sample.

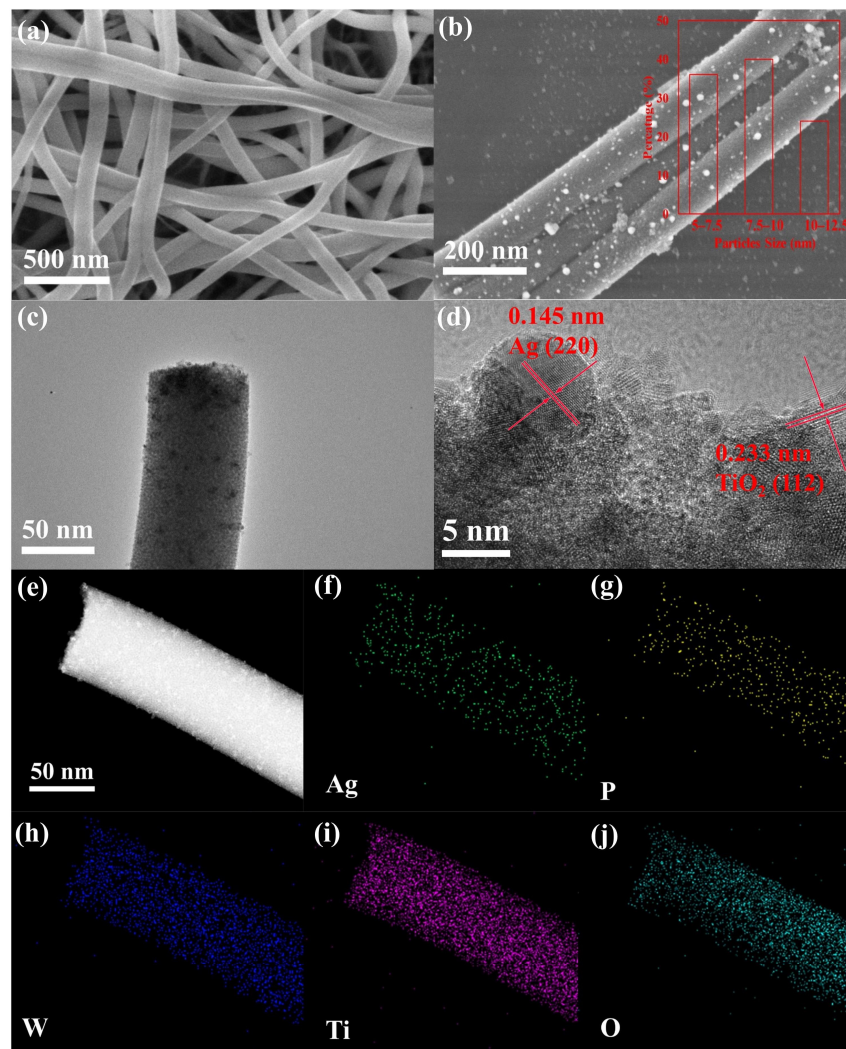


Figure 1. SEM images of PT (a) and 10% Ag/PT (b); TEM (c) and HRTEM (d) images of 10% Ag/PT; (e–j) Elemental mapping images of 10% Ag/PT sample: (f) Ag; (g) P; (h) W; (i) Ti; (j) O.

The phase composition and purity of the prepared catalysts were investigated with XRD (Figure 2a). For TiO_2 , these characteristic diffraction peaks at 25.3° , 36.9° , 37.8° , 38.5° , 48.0° , 53.9° , 55.0° , and 62.7° are attributed to the (101), (103), (004), (112), (200), (105), (211), and (204) crystal plane of anatase phase TiO_2 (JCPDS no. 21-1272), respectively [27,28]. With the introduction of PW_{12} into TiO_2 , no peaks of PW_{12} are found in the diffraction peaks of PT, demonstrating the doping of PW_{12} in TiO_2 . When Ag NPs are deposited on PT, the main diffraction peaks of Ag/PT composite are similar to those of PT. Additionally, the main diffraction peak at 38.1° , belonging to Ag (111) phase (JCPDS no. 04-0783), is not obviously found, which might be attributed to the cover effect with diffraction peak of PT [29]. The obtained results certify the presence of PT and Ag NPs in these Ag/PT composites.

Figure 2b displays the FT-IR spectra of various samples. TiO_2 has no obvious characteristic vibration peak, and the PW_{12} exhibits four characteristic infrared absorption peaks in $700\text{--}1100\text{ cm}^{-1}$, including the peaks at 1075 , 975 , 882 , and 830 cm^{-1} , respectively. Concretely, the peak at 1075 cm^{-1} is caused by the vibration of the P–O bond, the peak at 975 cm^{-1} is assigned to the vibration of the W=O bond, and the two peaks at

882 and 830 cm^{-1} are attributable to the vibration of the two kinds of $\text{W-O}_{\text{c/e}}\text{-W}$ bridge bonds [30,31]. Besides, the peak of PW_{12} near 1600 cm^{-1} may belong to the adsorbed H_2O molecules [32]. These peaks can be also observed in the PT and Ag/PT materials, indicating the integrity of the PW_{12} Keggin unit in these composites. However, a shift in the vibrational frequencies (1060, 961, 868, and 815 cm^{-1}) is detected for Ag/PT, manifesting the presence of interaction between PT and Ag [19]. The aforementioned results certify that the Ag/PT materials have been fabricated successfully.

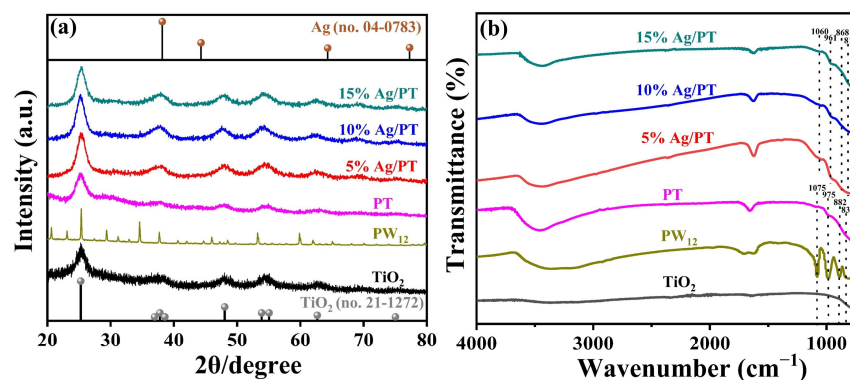


Figure 2. (a) XRD and (b) FT-IR of the constructed specimens.

A UV-Vis diffuse reflectance spectra (DRS) measurement was performed to evaluate the light absorption properties of the obtained specimens. According to Figure 3a, the light absorption edge of TiO_2 , PW_{12} catalysts appeared around 400 and 380 nm. For PT photocatalysts, the light absorption intensity was increased due to the adulteration of PW_{12} . In particular, the strongest optical absorption ability in the Ag/PT composites can be attributed to the introduction of Ag NPs [33], which would be beneficial to produce more photogenerated charge carriers to participate in the reaction [34]. We found that the SPR absorption band of Ag NPs ranges from 480 nm to 550 nm (Figure S2) [35]. Furthermore, as shown in Figure 3b, the band gaps of various catalysts were calculated by the following equation: $\alpha h\nu = A(h\nu - E_g)^{1/2}$, in which A , $h\nu$, and α represent the constant, photon energy, and absorption coefficient, respectively [36].

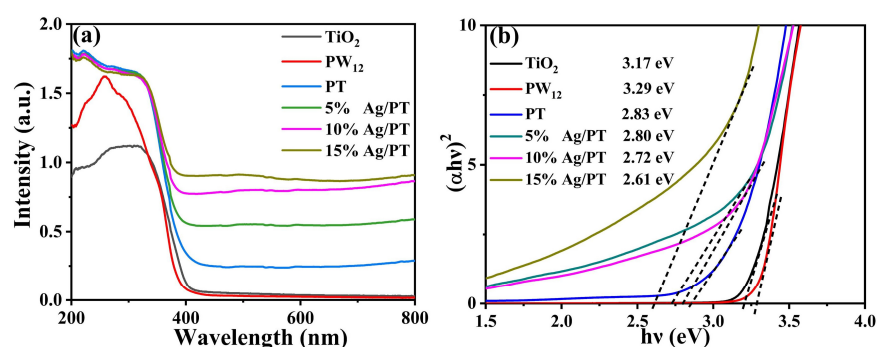


Figure 3. (a) UV-Vis absorption spectra and (b) the corresponding Tauc plots of obtained specimens.

The band gap values were 3.17, 3.29, 2.83, 2.80, 2.72, and 2.61 eV for TiO_2 , PW_{12} , PT, and $x\%$ Ag/PT ($x = 5, 10$ and 15), respectively. The doping of $\text{H}_3\text{PW}_{12}\text{O}_{40}$ introduces additional electronic states and energy levels into the band structure of TiO_2 . These additional electronic states can interact with the electron energy levels of TiO_2 , leading to adjustments in the band structure, thereby reducing the band gap [11,27]. Obviously, in comparison with PT, the band gap of Ag/PT was reduced, which suggests that Ag might introduce a local energy level to the band gap of PT, resulting in a reduced energy gap [37].

The composition and chemical state information of as-prepared specimens were probed with X-ray photoelectron spectroscopy (XPS). The elemental composition of

10% Ag/PT was demonstrated by the signal detection of P, W, O, Ti, and Ag elements in the full XPS spectra (Figure 4a). Figure 4b–f shows the high resolution XPS profiles for Ag 3d, P 2p, W 4f, Ti 2p, and O 1s of PT and 10% Ag/PT, confirming the successful preparation of the composites. As presented in Figure 4b, the 10% Ag/PT composite showed two peaks at Ag 3d, located at 367.61 eV and 373.59 eV, belonging to $\text{Ag}^0 3d_{5/2}$ and $\text{Ag}^0 3d_{3/2}$ metallic silver monomers, respectively [38,39]. The P 2p XPS profile for PT (Figure 4c) has a peak at 133.70 eV, and this binding energy was considered to be the presence of P^{5+} [40]. The P 2p peak of 10% Ag/PT was shifted towards the lower binding energy region in comparison with PT. In the PT material, the high-resolution XPS spectrum of the W 4f region (Figure 4d) showed two peaks at 35.58 eV and 37.63 eV for the W $4f_{7/2}$ and W $4f_{5/2}$ binding energies, respectively, and, in 10% Ag/PT, W 4f was shifted toward the lower binding energy with binding energies of 35.28 eV and 37.32 eV [41,42]. Figure 4e shows the presence of Ti $2p_{3/2}$ and Ti $2p_{1/2}$ characteristic peaks observed at 458.49 eV and 464.16 eV in PT, which are features of Ti^{4+} in TiO_2 [43]. Notably, the binding energies of Ti 2p XPS for 10% Ag/PT were shifted to 458.45 eV and 464.13 eV, providing evidence of the interaction between PT and Ag [44]. Figure 4f shows the XPS spectra of O 1s. Two peaks, at 529.57 eV (PT) and 529.48 eV (10% Ag/PT), were found, which were considered as Ti-O [45]; meanwhile, two peaks are found at 531.21 eV and 532.12 eV (PT) and 531.11 eV and 532.01 eV (10% Ag/PT), corresponding to W-O and P-O, respectively [46]. Notably, these peaks in 10% Ag/PT composites shifted to lower binding energies compared to PT, which indicated the presence of interfacial interaction between Ag and PT [47].

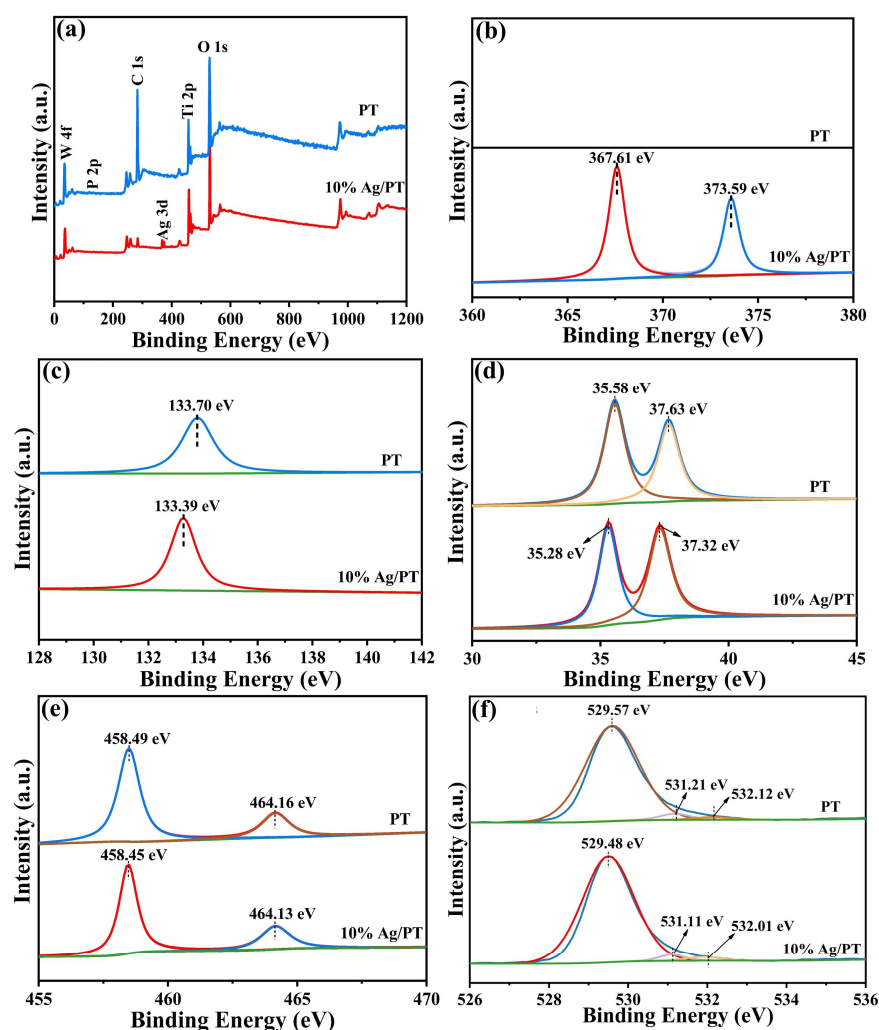


Figure 4. The XPS profiles: (a) full spectra; (b) Ag 3d; (c) P 2p; (d) W 4f; (e) Ti 2p; (f) O 1s.

Figure 5a demonstrates that the N_2 adsorption and desorption isotherms of different specimens conform to type IV, while the hysteresis line follows type H1, indicating the presence of a mesoporous structure [48,49]. The specific surface areas (SSA) were 30.39, 146.85, 156.42, 155.09, and 166.91 m^2/g for TiO_2 , PT and x% Ag/PT (x = 5, 10 and 15), respectively. The result suggested that the introduction of PW_{12} is beneficial to enhance the SSA of TiO_2 , which would demonstrate an improved catalytic performance. Figure 5b presents the pore size distributions of as-obtained samples. The average pore volumes were 11.57, 5.32, 4.25, 4.61, and 4.40 nm for TiO_2 , PT, and x% Ag/PT (x = 5, 10 and 15), respectively. It is clear that the average pore volume of Ag/PT composites decreased, which might be due to the accumulation of Ag NPs on the PT surface.

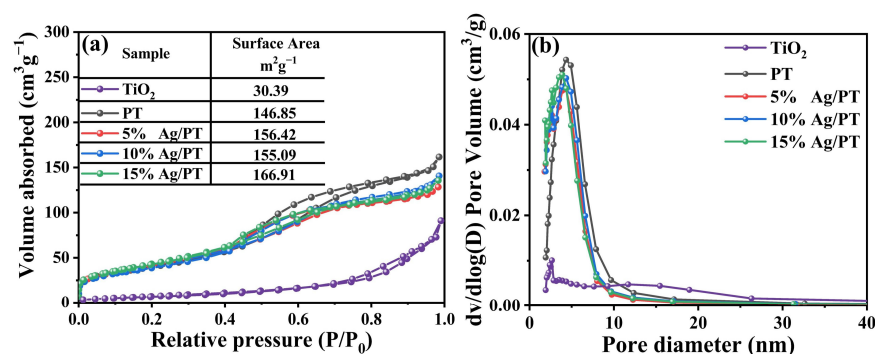


Figure 5. (a) N_2 adsorption-desorption isotherms and (b) pore size distributions of as-synthesized samples.

2.2. Catalytic Activity Assessment of Ag/PT Composites

2.2.1. Photocatalytic Removal of TC

TC was chosen as an organic pollutant to explore the photocatalytic capacity of obtained samples [50,51]. As presented in Figure 6a, the adsorption-desorption equilibrium was reached between the catalyst and TC under dark conditions within 20 min. The control experiment was designed and demonstrated that the self-photolysis process of TC can be excluded. TiO_2 exhibits a negative effect on the TC degradation. The degradation efficiencies of TC on PT and 10% Ag/ TiO_2 were significantly higher compared to pure TiO_2 , which reached 26.53% and 43.52% within 60 min, respectively. This indicates that the photocatalytic activity of TiO_2 can be improved with the proper introduction of $H_3PW_{12}O_{40}$ or Ag NPs. Moreover, the photocatalytic property of Ag/PT was further boosted, benefiting from the remarkable contribution of the SPR effect originating from the Ag NPs. The 10% Ag/PT composite shows the optimal degradation efficiency of 78.19% (Figure S3a), which exhibits better performance compared to numerous other catalysts, in terms of TC removal (Table S1). Besides, the removal of total organic carbon (TOC) for TC degradation reached 60.08% within 1 h using 10% Ag/PT material (Figure S4), which implies that the TC degradation was incomplete. Nevertheless, when more Ag was deposited on the PT, the TC removal rate of the synthesized 15% Ag/PT composite reduced to 71.12%. Because excessive Ag occupies a part of the active sites of PT, the adsorption capacity and degradation rate of Ag/PT composite towards TC molecules is reduced.

As presented in Figure 6b, the fitting results of the TC degradation rate indicate that it was in accordance with the first-order kinetic model. Distinguishingly, the reaction rate constant k for TC degradation with 10% Ag/PT was 0.0227 min^{-1} , which was about 29- and 8-times higher than those of TiO_2 and PT, respectively. Therefore, the doping of PW_{12} and the modification of Ag NPs are effective methods to boost the photocatalytic performance of TiO_2 .

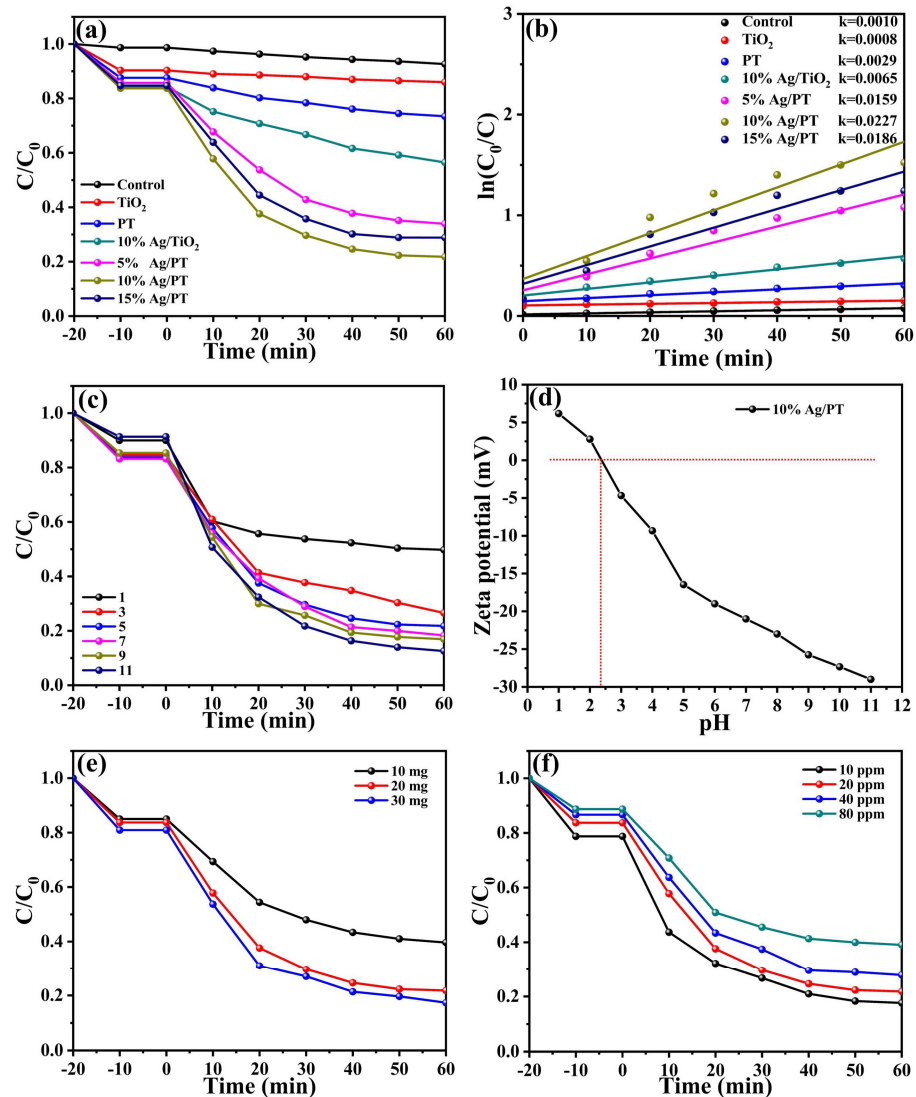


Figure 6. (a) The visible-light ($\lambda > 420$ nm) degradation of TC utilizing various specimens (catalyst usage: 20 mg; TC: 20 mL of 20 ppm; pH = 7); (b) The pseudo-first-order kinetic study for TC degradation; Degradation of TC with 10% Ag/PT with various conditions: (c) Different pH values (TC: 20 mL of 20 ppm; catalyst usage: 20 mg); (d) Zeta potential of 10% Ag/PT at different pH values; (e) Diverse catalyst amount (TC: 20 mL of 20 ppm; pH = 7); (f) Different concentration of TC (TC: 20 mL; pH = 7; catalyst amount: 20 mg). Light source: 300 W Xe light (CEL-HXF300, AULIGHT).

Effect of different pH values: The degradation of TC in aqueous solution undergoes protonation and deprotonation reactions, and the pH of the solution will lead to different charge states, which affects the decomposition of TC. As shown in Figure 6c, the TC degradation efficiency gradually increased with the increase of pH, which achieved the optimal value of 87.42% at pH 11. The alkaline environment favors the generation of $\bullet\text{O}_2^-$, which is one kind of active species during the pollutant degradation process [52]. Besides, TC molecules exhibit a high susceptibility to photolysis in alkaline conditions, benefiting from the transition from the π to π^* states of the (HOMO-1 to LUMO) chromophore [53]. At neutral pH, the TC removal rate was 78.19% after 60 min of light exposure. However, under acidic conditions, the degradation efficiency of TC further decreased. In Figure 6c, the adsorption removal efficiency of TC by 10% Ag/PT at different pH conditions were 10.04% (pH 1.0), 15.41% (pH 3.0), 16.28% (pH 5.0), 16.78% (pH 7.0), 14.61% (pH 9.0), and 8.67% (pH 11.0). This may be related to the zeta potential of the catalyst, which was examined for 10% Ag/PT at different pH conditions (Figure 6d). Obviously, the zeta

potential of 10% Ag/PT was positive at $\text{pH} < 2.4$ and negative at $\text{pH} > 2.4$. Moreover, when $\text{pH} < 3.3$, TC appeared as a cation (TCH_3^+); when $\text{pH} = 3.3\text{--}7.7$, TC existed as an ampholyte (TCH_2^0); when pH was greater than 7.7, TC appeared as an anion (TCH_3^-) [54]. Therefore, when $\text{pH} = 1.0$, the surface of 10% Ag/PT was positively charged and the TC molecules were present in the protonated (TCH_3^+ , $\text{pH} < 3.3$), which generated an intense electrostatic repulsion and weak adsorption ability. With the increase of pH from 3 to 7, the positive surface charge of 10% Ag/PT decreased from -4.64 mV to -21.07 mV, and the TC molecules were in neutral (TCH_2^0 , $\text{pH} 3.3\text{--}7.7$), indicating that the electrostatic repulsion was suppressed, thus promoting the adsorption capacity. When the pH was 9.0 and 11.0, the electrostatic repulsion existed between the catalyst with a negative charge and TC (TCH_3^- , $\text{pH} > 7.7$). Furthermore, the excess OH^- could occupy the adsorption sites of the catalyst, generating a slight reduction of adsorption ability [55].

Influence of catalyst dosage: As shown in Figure 6e, the degradation efficiency was significantly enhanced from 60.35% to 78.19%, with the catalyst quantity from 10 to 20 mg, which could be assigned to the increase of active sites [56]. However, the TC degradation rate increased indistinctively (78.19% to 82.64%) upon further increasing the catalyst usage from 20 to 30 mg, which may be due to the poor light transmission of the solution applying too much catalyst [57].

Effects of initial TC concentration: Figure 6f provides the effect of TC concentration on the photodegradation performance. The TC degradation rate decreased continuously, with the TC concentration ranging from 10 to 80 ppm. The explanation may be that the limited number of photogenerated carriers lead to restrict TC degradation when the initial TC concentration was too high. In addition, the higher TC concentration affected the penetration ability of photons and, thus, negatively affects the photocatalytic activity [58].

2.2.2. Photocatalytic Degradation of ENR and MO

The catalytic performance for Ag/PT composites were further evaluated by degrading ENR and MO in visible-light. During the dark reaction, the pollutants molecules were adsorbed on the photocatalyst surface for 20 min to obtain the adsorption-desorption equilibrium. As presented in Figure 7a, the photocatalytic degradation efficiencies of ENR with control, TiO_2 , 10% Ag/ TiO_2 , PT, 5% Ag/PT, 10% Ag/PT, and 15% Ag/PT were 1.99%, 20.17%, 58.84%, 63.09%, 87.93%, 93.65%, and 89.98%. Specially, 10% Ag/PT had the best photocatalytic activity of 93.65% ($k = 0.0194$) (Figures 7b and S3b), which was 4.64-, 1.48-, and 1.59-times higher than that of TiO_2 , 10% Ag/ TiO_2 , and PT, respectively. Similarly, the degradation profiles in Figure 7c manifesting 10% Ag/PT also displayed an excellent MO degradation rate of 99.29% ($k = 0.1549$) (Figures 7d and S3c). The influencing parameters of catalyst dosage and MO concentration were also studied in Figure S6. Moreover, the degradation efficiencies of Ag/PT composites are superior to other catalysts for ENR and MO removal (Tables S2 and S3). These data verify that as-prepared Ag/PT is one kind of multi-functional material in the field of environmental remediation.

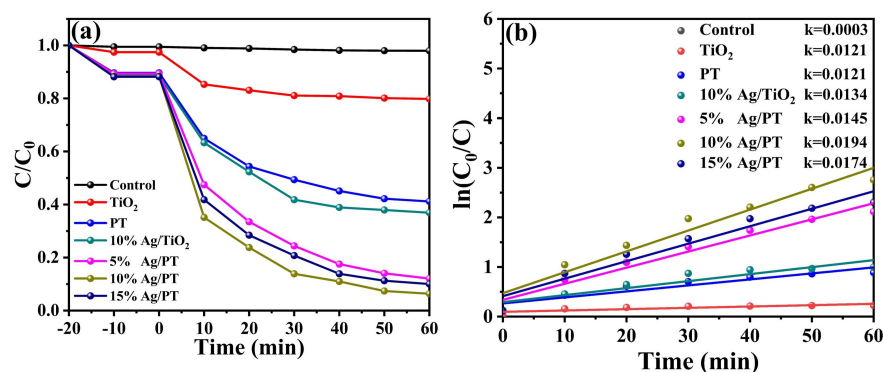


Figure 7. Cont.

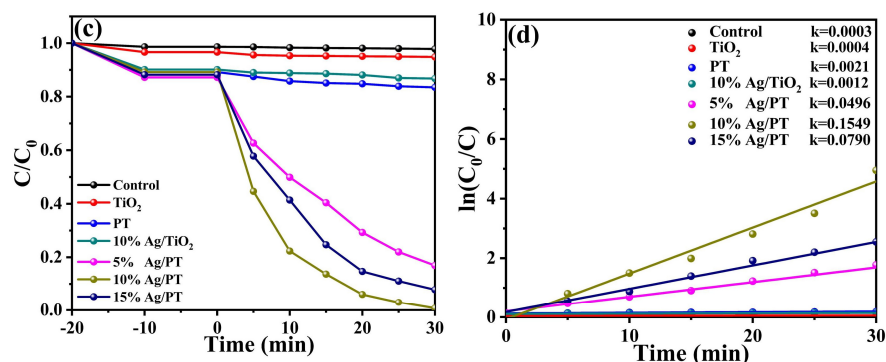


Figure 7. (a) Visible-light removal curves of ENR by different specimens; (b) Reaction rate constant k ; The degradation profiles (c) and reaction rate constant k (d) of MO degradation.

2.3. Stability Test of Photocatalyst

Figure 8a shows the cycling experiments of 10% Ag/PT as a visible-light catalyst for the degradation of various contaminants. After 20 cycles of reuse, the degradation efficiency of MO, ENR, and TC exhibited a slight decrease, and by using ICP-6000 test, the leaching amount of Ag after degradation was 2.1 ppm, indicating that the as-obtained Ag/PT composites had good reuse performance. Moreover, the photocatalytic stability of Ag/PT materials was confirmed with XRD and FT-IR. As shown in Figure 8b,c, the XRD diffraction peaks and FT-IR spectra of the used 10% Ag/PT remained unchanged in comparison with the fresh sample, verifying the good structural stability of these materials. Furthermore, the TEM image after TC removal (Figure 8d) also demonstrated the good cycling stability of the catalyst.

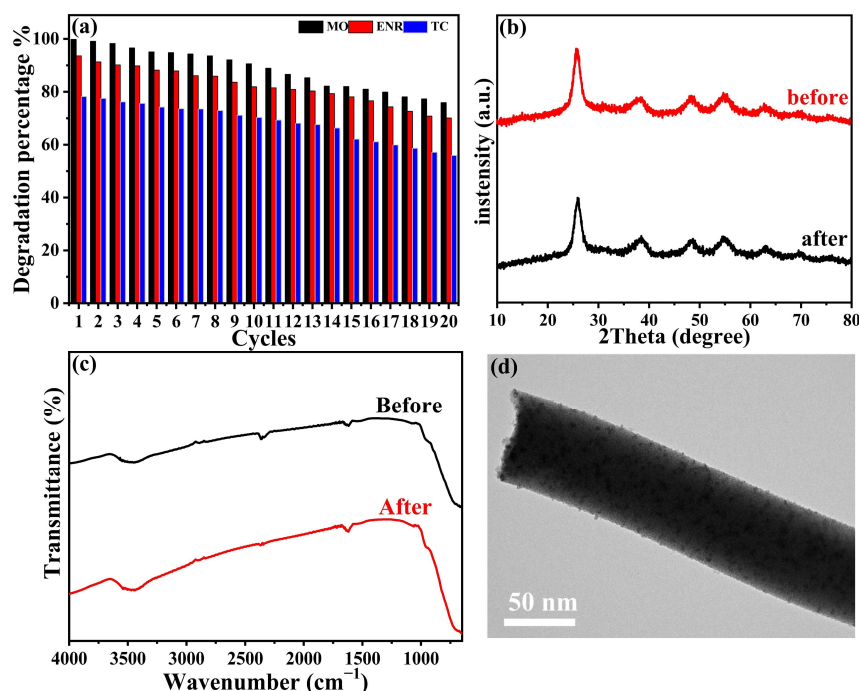


Figure 8. (a) The cyclic experiments for removing TC, ENR, and MO by 10% Ag/PT; XRD (b), FT-IR (c) TEM image (d) for 10% Ag/PT before and after use in TC degradation.

2.4. Photocatalytic Mechanism Investigation

2.4.1. Photogenerated Carriers Behavior Analysis

The photoluminescence (PL) spectra were measured to reflect the separation efficiency of photoinduced carriers from the synthesized catalysts. As demonstrated in Figure 9a, these materials exhibited similar peaks at 425 nm. The fluorescence intensity for

Ag/PT composite exhibited a significant decrease compared to TiO₂, PT, and 10% Ag/TiO₂, implying that the recombination of photogenerated charge carriers was effectively suppressed [59,60]. In addition, the 10% Ag/PT catalyst had the lowest peak intensity, implying a higher separation rate of electron-hole pairs and better catalytic capacity compared to the remaining specimens. The fluorescence lifetimes of PT and 10% Ag/PT were determined by time-resolved fluorescence attenuation spectrometry (TRPL). As revealed in Figure 9b, the fluorescence intensity of PT and 10% Ag/PT both decreased exponentially. The average fluorescence lifetime τ_{ave} of PT and 10% Ag/PT were calculated to be 0.18 ns and 0.06 ns, respectively (Table S4). The result shows that 10% Ag/PT has a shorter average decay time than PT, which indicates that the deposition of Ag nanoparticles is beneficial to delay the recombination of photoinduced carriers [61]. The corresponding quenching and lifetime reduction of TRPL implies a high non-radiative decay rate at 10% Ag/PT, and the establishment of a fast electron transfer pathway for accumulated photoproduced electrons is conducive to the enhancement of catalytic capacity [62].

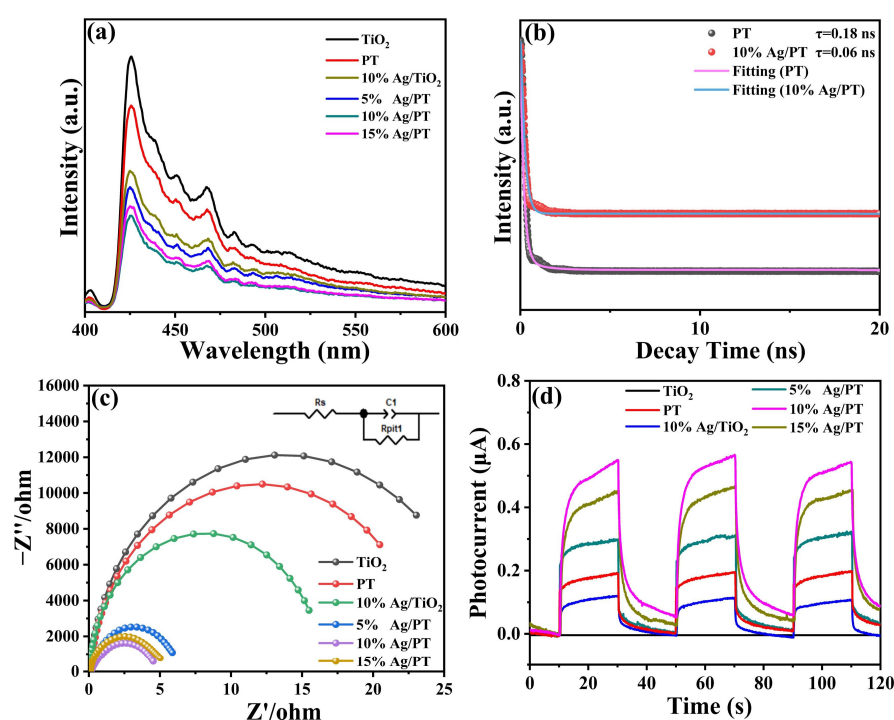


Figure 9. The steady PL (a), transient PL (b), EIS (Insert: impedance equivalent circuit diagram) (c) and photocurrent (d) of various samples.

The electrochemical impedance spectroscopy (EIS) and instantaneous photocurrent have been employed for examining the separation and migration ability of photogenerated electron-hole pairs. Figure 9c illustrates the EIS Nyquist plots from distinct electrodes, and the equivalent circuit are provided as an insert. Generally, the small EIS radius of the electrochemical impedance corresponds to the low charge transfer resist [63]. It is clear that the radius of these Ag/PT materials were much smaller than those of TiO₂, PT, and 10% Ag/TiO₂. Specially, 10% Ag/PT has the smallest radius, which strongly manifested that the composite possessed fastest transfer and migration ability of carriers [64]. Additionally, Figure S7 presents the Bode plots of PT and 10% Ag/PT, which confirmed a prolonged lifetime of photoinduced electrons for 10% Ag/PT in comparison to PT. The photocurrents of obtained specimens were measured in Figure 9d. The photocurrent was found to be stable and reproducible in three cycles. The photocurrent density obeyed the following order: 10% Ag/PT > 15% Ag/PT > 5% Ag/PT > 10% Ag/TiO₂ > PT > TiO₂. Specifically, the photocurrent density of 10% Ag/PT (0.23 $\mu\text{A}/\text{cm}^2$) was much larger than that of PT (0.09 $\mu\text{A}/\text{cm}^2$) and 10% Ag/TiO₂ (0.05 $\mu\text{A}/\text{cm}^2$), which would lead to a remarkable

enhancement in photocatalytic capability [65]. The results of various measurements collectively demonstrated that the Ag/PT composites have low charge transfer resistance and high separation efficiency of photogenerated carriers, which would reveal an outstanding catalytic performance.

2.4.2. Active Species in Photocatalytic Reactions

To elucidate the degradation mechanism of TC, the radical capture experiments were performed, and the results were presented in Figure 10a. Herein, 4-hydroxymethylpropane (TEMPO, $\cdot\text{O}_2^-$ quencher), triethanolamine (TEOA, h^+ quencher), and isopropyl alcohol (IPA, $\cdot\text{OH}$ quencher) were employed as free radical trapping agents [66,67]. Distinctly, the addition of TEOA to the reaction system significantly inhibited the degradation efficiency, and the addition of TEMPO also reduced the degradation activity to some extent, verifying the important function of h^+ and $\cdot\text{O}_2^-$ in TC degradation. Meanwhile, the degradation rate was almost unchanged with the addition of IPA, implying that $\cdot\text{OH}$ was not the dominating active substance.

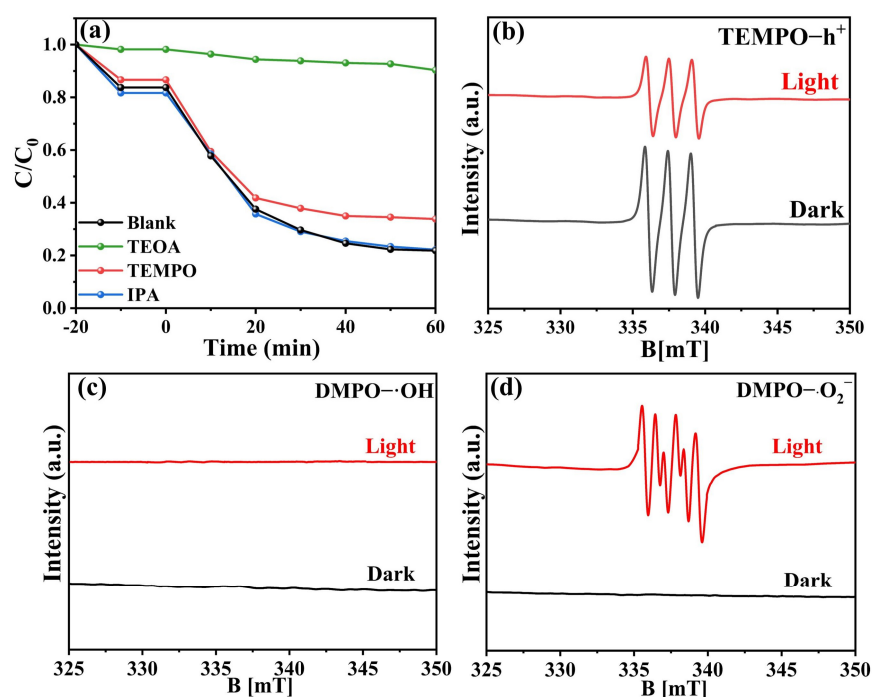


Figure 10. (a) The degradation of TC with diverse scavengers by 10% Ag/PT sample; (b) ESR spectra of TEMPO-h⁺; ESR signals of (c) DMPO- $\cdot\text{OH}$ and (d) DMPO- $\cdot\text{O}_2^-$.

To directly verify the reactive species involved in the reaction process, electron spin resonance (ESR) measurement was conducted, applying 5,5-dimethyl-1-pyrroline N-oxide (DMPO) and 2,2,6,6-Tetramethyl-1-piperidinyloxy (TEMPO) as spin-trapping agents [68]. TEMPO can trap the photogenerated holes and form⁺ TEMPO-h⁺ spin-products, which exhibit silent ESR signals. As displayed in Figure 10b, under dark conditions, three distinctive peaks corresponding to the TEMPO were identified, which were obviously declined under visible-light, demonstrating the production of TEMPO-h⁺ spin-products [69]. Meanwhile, $\cdot\text{OH}$ and $\cdot\text{O}_2^-$ can be captured with DMPO, generating evident ESR signals. In Figure 10c, no characteristic peaks were found under both dark and light conditions in the $\cdot\text{OH}$ test, indicating that $\cdot\text{OH}$ did not play a role in the catalytic reaction. In Figure 10d, in the $\cdot\text{O}_2^-$ test, no characteristic peaks were detected under dark conditions; nevertheless, the characteristic peaks corresponding to DMPO- $\cdot\text{O}_2^-$ were clearly observed upon visible-light irradiation, authenticating successful generation of $\cdot\text{O}_2^-$ radicals. These results indicated that the photodegradation of TC was primarily driven with the involvement of $\cdot\text{O}_2^-$ radicals and h^+ .

2.4.3. Degradation Pathways of TC and Toxicity Assessment

As revealed in Figures 11 and S5, the pathways of TC photodegradation were explored by HPLC-MS. The molecular weight of TC is expressed as the product $m/z = 444$. Figure 11 summarizes and illustrates two possible degradation pathways. In pathway 1, the intermediate of T1 ($m/z = 463$) may be derived from the dehydroxylation of TC, after which T1 forms T2 ($m/z = 403$) through the deamidation process. Intermediate with T3 ($m/z = 357$) is resulted from loss of one N-2 methyl group. The product T4 ($m/z = 259$) is obtained by the ring-opening reaction of T3. Pathway 2 is the transition from TC to T5 ($m/z = 427$) after deamination. Then, T5 is dehydroxylated and dedimethylated to T6 ($m/z = 398$), which is deaminated and demethylated to T7 ($m/z = 318$). After T4, T8 is formed by the break of double-bond oxygen, and T7 is formed by ring-opening and dehydroxylation. After continuous ring-opening reactions, T8 forms T9 ($m/z = 228$), T10 ($m/z = 182$), T11 ($m/z = 100$), and T12 ($m/z = 74$). Further degradation of intermediates can produce small molecules such as CO_2 , H_2O , and inorganic ions. According to the above analysis, it can be inferred that photocatalytic degradation of tetracycline involves deamidation, dehydroxylation, and ring-opening reactions [3,70].

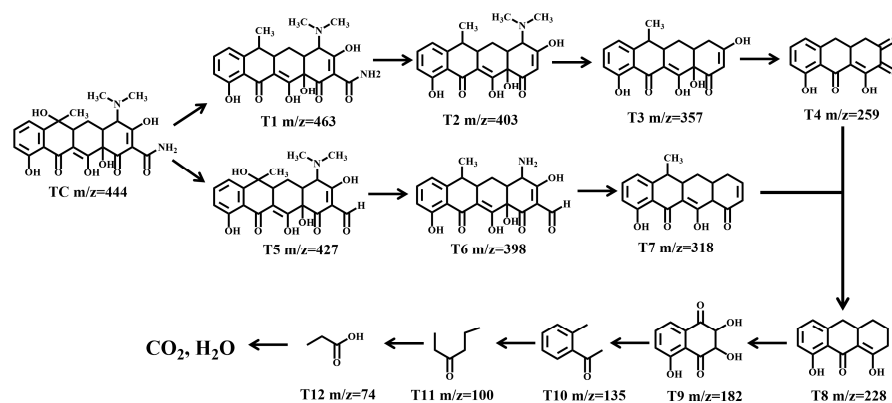


Figure 11. The probable catalytic degradation pathways for TC.

Furthermore, we investigated the toxicity of TC and its 12 intermediates using QSAR prediction with a toxicity estimation software tool (T.E.S.T. Version 5.1.2) [71]. Figure 12a,b show that TC was “developmentally toxic” and “mutagenic positive” [72]. One developmentally non-toxic TC intermediate (T10) and four mutagenic-negative TC intermediates (T7, T10, T11, T12) were produced after light treatment. Furthermore, most intermediates were less toxic than TC. As illustrated in Figure 12c, the bioaccumulation factors of intermediates T9 and T6 were lower than those of TC, and the photodegradation process could reduce the bioaccumulation factor for TC, which was primarily attributed to the hydroxylation reaction [73].

In Figure 12d–f, three evaluation indicators were used to evaluate the acute toxicity of TC and its intermediates: (i) Fathead minnow LC_{50} (96 h) represents the concentration at which 50% of fathead minnows are killed after 96 h; (ii) *Daphnia magna* LC_{50} (48 h) represents the concentration at which 50% of *Daphnia magna* are killed after 48 h; and (iii) Oral rats LD_{50} represents the concentration at which 50% of rats are killed after 48 h of oral ingestion. The LC_{50} values of 0.90 mg/L for blackhead minnow, 12.70 mg/L for *Daphnia magna*, and 1105.75 mg/kg for TC in rats were defined as “highly toxic”, “harmful”, and “toxic” compounds, respectively [74]. Obviously, T1, T6, T7, and T8 intermediates all showed low LD_{50} values (Figure 12d). *Daphnia magna* showed lower LC_{50} values than TC intermediates, except for T6, T7, T1, T2, T3, and T8 (Figure 12e). With the exception of intermediates T5 and T11, rats exhibited lower toxicity to TC intermediates (Figure 12f). According to the aforementioned toxicity prediction results, the toxicity of several intermediates still exists, which could be reduced by extending the reaction time.

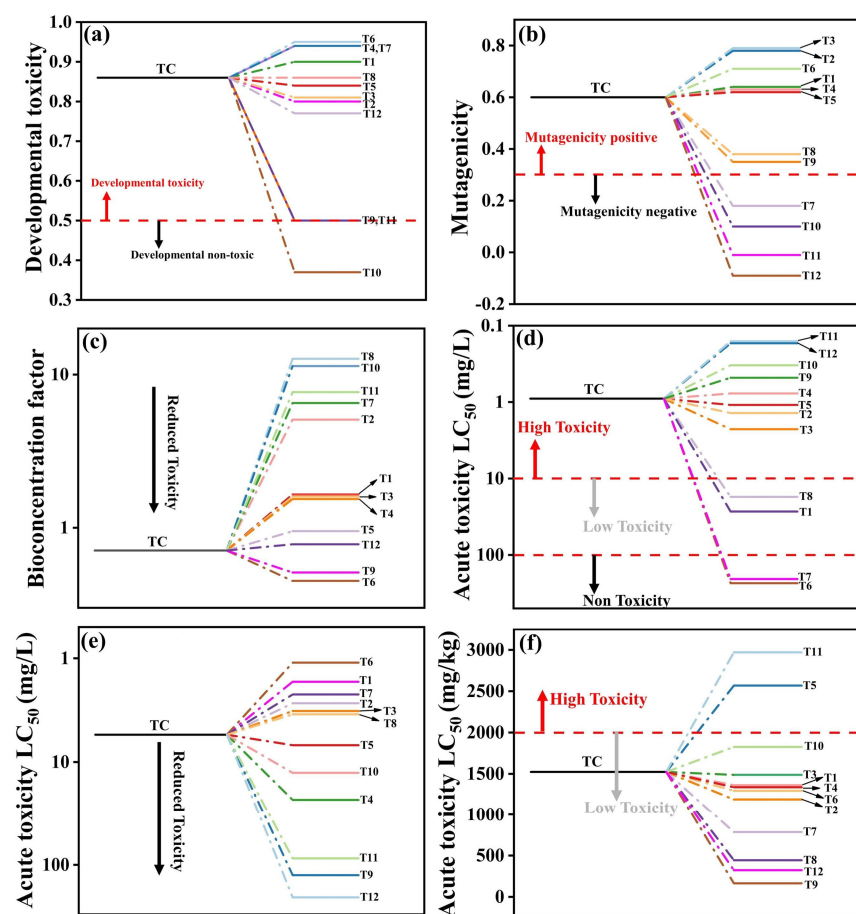
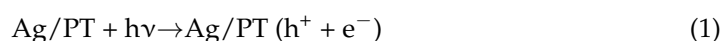


Figure 12. (a) Developmental toxicity; (b) mutagenicity; (c) bioconcentration factor; (d) fathead minnow, (e) *Daphnia magna* (f), and oral rat for these products in TC degradation.

2.4.4. Possible Photocatalytic Mechanism

In Figure S9, the tangent slope of the Mott-Schottky profile reflects that PT belongs to n-type semiconductor. The E_{fb} of PT relative to Hg/Hg_2Cl_2 was found to be -0.17 eV. Given that the conduction band energy (E_{CB}) of n-type semiconductor is approximately 0.2 eV higher than the flat band potential (E_{fb}) [75], the E_{CB} for PT could be determined as -0.13 eV (vs. NHE), according to $E_{NHE} = E_{Hg/Hg_2Cl_2} + 0.242$ eV. From the $(\alpha hv)^2$ vs. hv plot (Figure 3b), the band gap energy (E_g) of PT is calculated to be 2.83 eV. Therefore, the VB (valence band) edge position of PT ($E_{VB} = E_{CB} + E_g$) is determined to be 2.70 eV [76]. Based on the aforementioned results, the catalytic mechanism for TC degradation by Ag/PT system with visible-light was proposed (Figure 13). The PT was photoexcited to generate electrons and holes under visible-light irradiation (Equation (1)). Meanwhile, a large number of hot electrons are produced, due to the surface plasmon resonance (SPR) effect of Ag NPs [77,78]. The Ag NPs serving as electron traps could effectively capture photoinduced electrons on the CB of PT, while the Schottky barrier established by Ag^0 could promote the transfer of SPR-excited electrons, further accelerating the charge separation (Equation (2)). These electrons on Ag NPs react with O_2 to form $\cdot O_2^-$ participating in oxidation reaction (Equations (3) and (4)). Moreover, the photoinduced holes in PT directly oxidize TC according to the result of ESR measurements and capturing tests (Equation (5)). Ultimately, TC was efficiently removed with the help of h^+ and $\cdot O_2^-$ active species (Equation (6)).



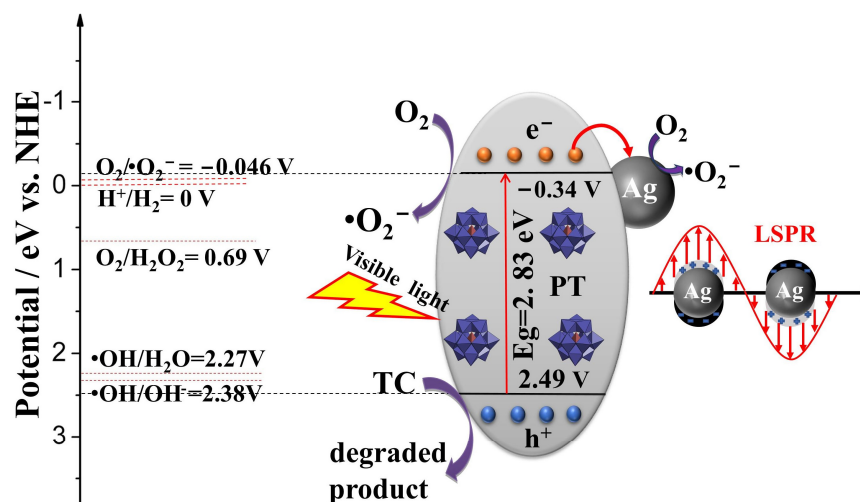
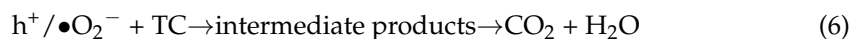
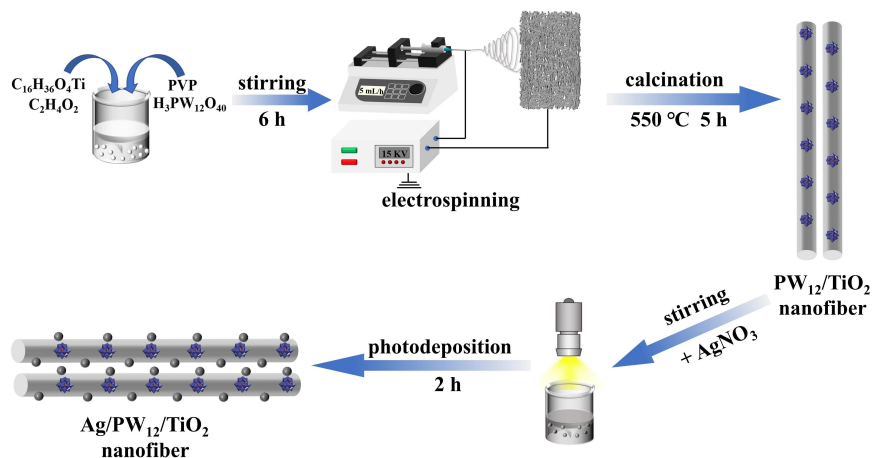


Figure 13. The photocatalytic mechanism of TC degradation using Ag/PT system.

3. Experiments and Characterizations

Construction of Ag/PT Photocatalysts

As shown in Scheme 1, Ag/PT composite nanofibers were prepared employing electrospinning/photoreduction methods. First of all, PT nanofibers were synthesized by the electrospinning/calcination method. Briefly, PVP was dissolved in a mixture of anhydrous ethanol, acetic acid, and tetrabutyl titanate, and stirred for 1 h. PW_{12} was then added and stirred until complete dissolution. The homogeneous precursor solution was subjected to electrostatic spinning operation, followed by calcination, to prepare PT nanofibers. Secondly, Ag NPs were modified on the PT nanofibers by photoreduction. PT nanofibers powder was added to the solution of $V_{\text{water}}:V_{\text{isopropanol}} = 1:1$, which was then sonicated for 30 min. Then, the solution was evacuated, and the suspension was illuminated for 1 h using a 300 W xenon lamp with full spectrum light. Then, AgNO_3 solution was added and stirred for 60 min. The Ag/PT composite was prepared.



Scheme 1. Schematic diagram for the fabrication process of Ag/PT composite.

The fabrication and characterization methods of Ag/PT composites are displayed in the Supplementary Material.

4. Conclusions

Herein, a novel Ag/PT composite material has been constructed utilizing electrospinning/photoreduction methods, which exhibited remarkable photocatalytic activities for degradation TC, ENR, and MO. The results of mechanism investigation showed that the excellent catalytic property could be due to the following two reasons: (1) the doping of PW_{12} to TiO_2 can enhance the utilization of visible spectrum and redox reaction activity of titanium dioxide; (2) the precious metal Ag possesses the LSPR effect, which can improve the utilization of sunlight and generate more charge carriers. Besides, the LSPR effect will have a high-intensity small range electromagnetic field, which will greatly improve the separation rate of photogenerated electron-hole pairs. Moreover, the degradation intermediates and pathways were revealed through HPLC-MS. The toxicity of TC degradation products was also investigated using QSAR prediction. This current work offers novel thoughts for developing efficient and stable catalysts for environmental remediation.

Supplementary Materials: The following supporting information can be downloaded at: <https://www.mdpi.com/article/10.3390/molecules28196831/s1>, Figure S1: EDX data of 10% Ag/PT sample; Figure S2: UV-Vis absorption spectra of 5%, 10% and 15% Ag/PT sample; Figure S3: The profiles of photocatalytic degradation of TC (a), ENR (b) and MO (c) by 10% Ag/PT under visible-light irradiation ($\lambda > 420$ nm); Figure S4: The TOC removal (%) for TC degradation by 10% Ag/PT sample; Figure S5: Photodegradation of TC with 10% Ag/PT under Diverse water quality (catalyst amount: 20 mg; TC: 20 mL of 20 ppm; pH = 7). Figure S6: Degradation of MO with 10% Ag/PT with various conditions: (a) Diverse catalyst amount (MO: 20 mL of 20 ppm; pH = 1) and (b) Different concentration of MO (MO: 20 mL; pH = 1; catalyst amount: 20 mg). Figure S7: The Bode plots of PT and 10% Ag/PT composite; Figure S8: The main intermediate products generated during the photocatalytic TC degradation process: (a) 0 min; (b) 30 min; (c) 60 min with 10% Ag/PT as catalyst; Figure S9: The E_{fb} of PT (V vs. Hg/Hg_2Cl_2). Table S1: The comparison of TC degradation activity of 10% Ag/PT with previous literatures; Table S2: The comparison of ENR degradation activity of 10% Ag/PT with previous literatures; Table S3: The comparison of MO degradation activity of 10% Ag/PT with previous literatures; Table S4: Fitted parameters of the TRPL decay profiles. References [79–122] are cited in the Supplementary Materials.

Author Contributions: Conceptualization, H.S.; methodology, H.W.; validation, H.W., E.Z., S.Z. and H.G.; investigation, E.Z. and H.G.; resources, H.S. and J.L.; writing—original draft preparation, H.W. and E.Z.; writing—review and editing, H.S.; funding acquisition, H.S., X.Q., J.L., S.Z. and Z.C.; supervision, Z.C.; Software, H.W. All authors have read and agreed to the published version of the manuscript.

Funding: The work was financially supported with the Natural Science Foundation of Jilin Province (YDZJ202201ZYTS360, YDZJ202201ZYTS358, YDZJ202201ZYTS591), the Project of Jilin Provincial Department of Education (JJKH20210233KJ) and the National Natural Science Foundation of China (22309061, 22278172, 22071080, 22109105).

Institutional Review Board Statement: Not applicable.

Informed Consent Statement: Not applicable.

Data Availability Statement: Data are contained within the article and Supplementary Materials.

Acknowledgments: The authors would like to acknowledge the technical support from JLICT CCA.

Conflicts of Interest: The authors declare no conflict of interest.

Sample Availability: Samples of the compounds are available from the authors.

References

1. Wu, Z.; Wang, M.Y.; Bai, Y.; Song, H.; Lv, J.X.; Mo, X.F.; Li, X.Q.; Lin, Z. Upcycling of nickel iron slags to hierarchical self-assembled flower-like photocatalysts for highly efficient degradation of high-concentration tetracycline. *Chem. Eng. J.* **2023**, *464*, 142532. [[CrossRef](#)]
2. Miao, Y.X.; Zhao, Y.X.; Zhang, S.; Shi, R.; Zhang, T.R. Strain engineering: A boosting strategy for photocatalysis. *Adv. Mater.* **2022**, *34*, 2200868. [[CrossRef](#)] [[PubMed](#)]
3. Li, B.; Tong, F.X.; Lv, M.; Wang, Z.Y.; Liu, Y.Y.; Wang, P.; Cheng, H.F.; Dai, Y.; Zheng, Z.K.; Huang, B.B. In situ monitoring charge transfer on topotactic epitaxial heterointerface for tetracycline degradation at the single-particle level. *ACS Catal.* **2022**, *12*, 9114–9124. [[CrossRef](#)]
4. Liccardo, L.; Bordin, M.; Sheverdyeva, P.M.; Belli, M.; Moras, P.; Vomiero, A.; Moretti, E. Surface defect engineering in colored TiO₂ hollow spheres toward efficient photocatalysis. *Adv. Funct. Mater.* **2023**, *33*, 2212486. [[CrossRef](#)]
5. Cao, H.; Liu, F.Y.; Tai, Y.T.; Wang, W.; Li, X.Y.; Li, P.Y.; Zhao, H.Z.; Xia, Y.Q.; Wang, S.J. Promoting photocatalytic performance of TiO₂ nanomaterials by structural and electronic modulation. *Chem. Eng. J.* **2023**, *466*, 143219. [[CrossRef](#)]
6. Zhu, Y.; Wang, D.; Huang, Q.; Du, J.; Sun, L.; Li, F.; Meyer, T.J. Stabilization of a molecular water oxidation catalyst on a dye-sensitized photoanode by apyridyl anchor. *Nat. Commun.* **2020**, *11*, 4610. [[CrossRef](#)]
7. Xing, F.Y.; Wang, C.Z.; Liu, S.Q.; Jin, S.H.; Jin, H.B.; Li, J.B. Interfacial chemical bond engineering in a direct Z-Scheme g-C₃N₄/MoS₂ heterojunction. *ACS Appl. Mater. Interface* **2023**, *15*, 11731–11740. [[CrossRef](#)]
8. Sun, G.T.; Tai, Z.G.; Li, F.; Ye, Q.; Wang, T.; Fang, Z.Y.; Jia, L.C.; Liu, W.; Wang, H.Q. Construction of ZnIn₂S₄/CdS/PdS S-Scheme heterostructure for efficient photocatalytic H₂ production. *Small* **2023**, *19*, 2207758. [[CrossRef](#)]
9. Zhao, X.Y.; Zhang, Y.; Zhao, Y.N.; Tan, H.Q.; Zhao, Z.; Shi, H.F.; Wang, E.B.; Li, Y.G. Ag_xH_{3-x}PMO₁₂O₄₀/Ag nanorods/g-C₃N₄ 1D/2D Z-scheme heterojunction for highly efficient visible-light photocatalysis. *Dalton Trans.* **2019**, *48*, 6484–6491. [[CrossRef](#)]
10. Horn, M.R.; Singh, A.; Alomari, S.; Goberna-Ferrón, S.; Benages-Vilau, R.; Chodankar, N.; Motta, N.; Ostrikov, K.; MacLeod, J.; Sonar, P.; et al. Polyoxometalates (POMs): From electroactive clusters to energy materials. *Energy Environ. Sci.* **2021**, *14*, 1652–1700. [[CrossRef](#)]
11. Shi, H.F.; Yu, Y.C.; Zhang, Y.; Feng, X.J.; Zhao, X.Y.; Tan, H.Q.; Khan, S.U.; Li, Y.G.; Wang, E.B. Polyoxometalate/TiO₂/Ag composite nanofibers with enhanced photocatalytic performance under visible light. *Appl. Catal. B-Environ.* **2018**, *221*, 280–289. [[CrossRef](#)]
12. Chen, L.; Chen, W.L.; Wang, X.L.; Li, Y.G.; Su, Z.M.; Wang, E.B. Polyoxometalates in dye-sensitized solar cells. *Chem. Soc. Rev.* **2019**, *48*, 260–284. [[CrossRef](#)] [[PubMed](#)]
13. Mirzaei, M.; Eshtiagh-Hosseini, H.; Alipour, M.; Frontera, A. Recent developments in the crystal engineering of diverse coordination modes (0–12) for Keggin-type polyoxometalates in hybrid inorganic-organic architectures. *Coord. Chem. Rev.* **2014**, *275*, 1–18. [[CrossRef](#)]
14. Xing, F.S.; Zeng, R.Y.; Cheng, C.C.; Liu, Q.W.; Huang, C.J. POM-incorporated ZnIn₂S₄ Z-scheme dual-functional photocatalysts for cooperative benzyl alcohol oxidation and H₂ evolution in aqueous solution. *Appl. Catal. B Environ.* **2022**, *306*, 121087. [[CrossRef](#)]
15. Yu, B.; Zhang, S.M.; Wang, X. Helical microporous nanorods assembled by polyoxometalate clusters for the photocatalytic oxidation of toluene. *Angew. Chem. Int. Ed.* **2021**, *60*, 17404–17409. [[CrossRef](#)] [[PubMed](#)]
16. Li, Y.S.; Liu, M.X.; Chen, L. Polyoxometalate built-in conjugated microporous polymers for visible-light heterogeneous photocatalysis. *J. Mater. Chem. A* **2017**, *5*, 13757–13762. [[CrossRef](#)]
17. He, B.W.; Luo, C.; Wang, Z.L.; Zhang, L.Y.; Yu, J.G. Synergistic enhancement of solar H₂O₂ and HCOOH production over TiO₂ by dual co-catalyst loading in a tri-phase system. *Appl. Catal. B-Environ.* **2023**, *323*, 122200. [[CrossRef](#)]
18. Pellejero, I.; Clemente, A.; Reinoso, S.; Cornejo, A.; Navajas, A.; Vesperinas, J.J.; Urbiztondo, M.A.; Gandía, L.M. Innovative catalyst integration on transparent silicone microreactors for photocatalytic applications. *Catal. Today* **2022**, *383*, 164–172. [[CrossRef](#)]
19. Shi, H.F.; Zhao, T.T.; Zhang, Y.; Tan, H.Q.; Shen, W.H.; Wang, W.D.; Li, Y.G.; Wang, E.B. Pt/POMs/TiO₂ composite nanofibers with enhanced visible-light photocatalytic performance for environmental remediation. *Dalton Trans.* **2019**, *48*, 13353–13359. [[CrossRef](#)]
20. Chen, X.; Wang, Z.P.; Shen, X.C.; Zhang, Y.; Lou, Y.; Pan, C.S.; Zhu, Y.F.; Xu, J. A plasmonic Z-scheme Ag@AgCl/PDI photocatalyst for the efficient elimination of organic pollutants, antibiotic resistant bacteria and antibiotic resistance genes. *Appl. Catal. B-Environ.* **2023**, *324*, 122220. [[CrossRef](#)]
21. Xu, Z.Y.; Guo, C.Y.; Liu, X.; Li, L.; Wang, L.; Xu, H.L.; Zhang, D.K.; Li, C.H.; Li, Q.; Wang, W.T. Ag nanoparticles anchored organic/inorganic Z-scheme 3DOMM-TiO_{2-x}-based heterojunction for efficient photocatalytic and photoelectrochemical water splitting. *Chin. J. Catal.* **2022**, *43*, 1360–1370. [[CrossRef](#)]
22. Zeng, Q.L.; Xie, X.F.; Wang, X.; Wang, Y.; Lu, G.H.; Pui, D.Y.H.; Sun, J. Enhanced photocatalytic performance of Ag@TiO₂ for the gaseous acetaldehyde photodegradation under fluorescent lamp. *Chem. Eng. J.* **2018**, *341*, 83–92. [[CrossRef](#)]
23. Kumar, P.S.; Sundaramurthy, J.; Sundarajan, S.; Babu, V.J.; Singh, G.; Allakhverdiev, S.I.; Ramakrishna, S. Hierarchical electrospun nanofibers for energy harvesting, production and environmental remediation. *Energy Environ. Sci.* **2014**, *7*, 3192–3222. [[CrossRef](#)]
24. Li, C.X.; Zhao, Y.X.; Song, Y.X.; Qiu, X.J.; Wang, S.Z.; Sun, P.Z. Optimization of electron transport pathway: A novel strategy to solve the photocorrosion of Ag-based photocatalysts. *Environ. Sci. Technol.* **2023**. [[CrossRef](#)] [[PubMed](#)]

25. Zhang, J.M.; Jiang, X.Y.; Huang, J.D.; Lu, W.; Zhang, Z.Y. Plasmon-enhanced photocatalytic overall water-splitting over Au nanoparticle-decorated CaNb_2O_6 electrospun nanofibers. *J. Mater. Chem. A* **2022**, *10*, 20048–20058. [[CrossRef](#)]
26. Le, T.T.; Lee, M.; Chae, K.H.; Moon, G.H.; Kim, S.H. Control of copper element in mesoporous iron oxide photocatalysts towards UV light-assisted superfast mineralization of isopropyl alcohol with peroxydisulfate. *Chem. Eng. J.* **2023**, *451*, 139048. [[CrossRef](#)]
27. Shi, H.F.; Zhao, T.T.; Wang, J.B.; Wang, Y.T.; Chen, Z.; Liu, B.L.; Ji, H.F.; Wang, W.D.; Zhang, G.L.; Li, Y.G. Fabrication of $\text{g-C}_3\text{N}_4/\text{PW}_{12}/\text{TiO}_2$ composite with significantly enhanced photocatalytic performance under visible light. *J. Alloys Compd.* **2021**, *860*, 157924. [[CrossRef](#)]
28. Mahadadalkar, M.A.; Park, N.; Yusuf, M.; Nagappan, S.; Nallal, M.; Park, K.H. Electrospun Fe doped TiO_2 fiber photocatalyst for efficient wastewater treatment. *Chemosphere* **2023**, *330*, 138599. [[CrossRef](#)]
29. Ni, J.X.; Liu, D.M.; Wang, W.; Wang, A.W.; Jia, J.L.; Tian, J.Y.; Xing, Z.P. Hierarchical defect-rich flower-like BiOBr/Ag nanoparticles/ultrathin $\text{g-C}_3\text{N}_4$ with transfer channels plasmonic Z-scheme heterojunction photocatalyst for accelerated visible-light-driven photothermal-photocatalytic oxytetracycline degradation. *Chem. Eng. J.* **2021**, *419*, 129969. [[CrossRef](#)]
30. Huang, X.Y.; Liu, X. Highly polymerized linear polyimide/ $\text{H}_3\text{PW}_{12}\text{O}_{40}$ photocatalyst with full visible light region absorption. *Chemosphere* **2021**, *283*, 131230. [[CrossRef](#)]
31. You, Y.L.J.; Gao, S.Y.; Yang, Z.; Cao, M.N.; Cao, R. Facile synthesis of polyoxometalate-thionine composite via direct precipitation method and its photocatalytic activity for degradation of rhodamine B under visible light. *J. Colloid Interface Sci.* **2012**, *365*, 198–203. [[CrossRef](#)] [[PubMed](#)]
32. Song, Y.B.; Guo, Y.M.; Qi, S.P.; Zhang, K.; Yang, J.F.; Li, B.N.; Chen, J.X.; Zhao, Y.X.; Lou, Y.B. $\text{Cu}_7\text{S}_4/\text{MnIn}_2\text{S}_4$ heterojunction for efficient photocatalytic hydrogen generation. *J. Alloys Compd.* **2021**, *884*, 161035. [[CrossRef](#)]
33. Gao, B.Q.; Tao, K.K.; Xi, Z.H.; El-Sayed, M.M.H.; Shoeib, T.; Yang, H. Fabrication of 3D lignosulfonate composited sponges impregnated by $\text{BiVO}_4/\text{polyaniline}/\text{Ag}$ ternary photocatalyst for synergistic adsorption-photodegradation of fluoroquinolones in water. *Chem. Eng. J.* **2022**, *446*, 137282. [[CrossRef](#)]
34. Kong, W.H.; Wang, S.L.; Wu, D.; Chen, C.R.; Luo, Y.S.; Pei, Y.T.; Tian, B.Z.; Zhang, J.L. Fabrication of 3D sponge@ $\text{AgBr-AgCl}/\text{Ag}$ and tubular photoreactor for continuous wastewater purification under sunlight irradiation. *ACS Sustain. Chem. Eng.* **2019**, *7*, 14051–14063. [[CrossRef](#)]
35. Tamilselvan, S.; Soniya, R.M.; Vasantharaja, R.; Kannan, M.; Supriya, S. Silver nanoparticles based spectroscopic sensing of eight metal ions in aqueous solutions. *Environ. Res.* **2022**, *212*, 113585. [[CrossRef](#)]
36. Shi, H.F.; Jin, T.; Li, J.P.; Li, Y.L.; Chang, Y.Q.; Jin, Z.H.; Jiang, W.; Qu, X.S.; Chen, Z. Construction of Z-scheme $\text{Cs}_3\text{PMo}_{12}\text{O}_{40}/\text{g-C}_3\text{N}_4$ composite photocatalyst with highly efficient photocatalytic performance under visible light irradiation. *J. Solid State Chem.* **2022**, *311*, 123069. [[CrossRef](#)]
37. Devi, L.G.; Kavitha, R. A review on plasmonic metal– TiO_2 composite for generation, trapping, storing and dynamic vectorial transfer of photogenerated electrons across the Schottky junction in a photocatalytic system. *Appl. Surf. Sci.* **2016**, *360*, 601–622. [[CrossRef](#)]
38. Mu, F.H.; Liu, C.X.; Xie, Y.; Zhou, S.J.; Dai, B.L.; Xia, D.H.; Huang, H.B.; Zhao, W.; Sun, C.; Kong, Y.; et al. Metal-organic framework-derived rodlike $\text{AgCl}/\text{Ag}/\text{In}_2\text{O}_3$: A plasmonic Z-scheme visible light photocatalyst. *Chem. Eng. J.* **2021**, *415*, 129010. [[CrossRef](#)]
39. Basumatary, B.; Basumatary, R.; Ramchiary, A.; Konwar, D. Evaluation of $\text{Ag@TiO}_2/\text{WO}_3$ heterojunction photocatalyst for enhanced photocatalytic activity towards methylene blue degradation. *Chemosphere* **2022**, *286*, 131848. [[CrossRef](#)]
40. Yang, R.X.; Zhong, S.; Zhang, L.S.; Liu, B.J. $\text{PW}_{12}/\text{CN@Bi}_2\text{WO}_6$ composite photocatalyst prepared based on organic-inorganic hybrid system for removing pollutants in water. *Sep. Purif. Technol.* **2020**, *235*, 116270. [[CrossRef](#)]
41. Lu, N.; Wang, Y.Q.; Ning, S.Q.; Zhao, W.J.; Qian, M.; Ma, Y.; Wang, J.; Fan, L.Y.; Guan, J.N.; Yuan, X. Design of plasmonic $\text{Ag-TiO}_2/\text{H}_3\text{PW}_{12}\text{O}_{40}$ composite film with enhanced sunlight photocatalytic activity towards o-chlorophenol degradation. *Sci. Rep.* **2017**, *7*, 17298. [[CrossRef](#)] [[PubMed](#)]
42. Yang, X.; Li, M.H.; Xu, L.; Li, F.Y. Limitation of WO_3 in $\text{Zn-Co}_3\text{O}_4$ nanopolyhedra by the pyrolysis of $\text{H}_3\text{PW}_{12}\text{O}_{40}@BMZIF$: Synergistic effect of heterostructure and oxygen vacancies for enhanced nitrogen fixation. *Inorg. Chem.* **2023**, *62*, 8710–8718. [[CrossRef](#)] [[PubMed](#)]
43. Chen, Z.; Chen, H.X.; Wang, K.; Chen, J.; Li, M.; Wang, Y.; Tsiakaras, P.; Song, S.Q. Enhanced TiO_2 photocatalytic 2e^- oxygen reduction reaction via interfacial microenvironment regulation and mechanism analysis. *ACS Catal.* **2023**, *13*, 6497–6508. [[CrossRef](#)]
44. Gao, Y.T.; Chen, F.; Chen, Z.; Shi, H.F. $\text{Ni}_x\text{Co}_{1-x}\text{S}$ as an effective noble metal-free cocatalyst for enhanced photocatalytic activity of $\text{g-C}_3\text{N}_4$. *J. Mater. Sci. Technol.* **2020**, *56*, 227–235. [[CrossRef](#)]
45. Guo, J.; Gan, W.; Ding, C.S.; Lu, Y.Q.; Li, J.R.; Qi, S.H.; Zhang, M.; Sun, Z.Q. Black phosphorus quantum dots and Ag nanoparticles co-modified TiO_2 nanorod arrays as powerful photocatalyst for tetracycline hydrochloride degradation: Pathways, toxicity assessment, and mechanism insight. *Sep. Purif. Technol.* **2022**, *297*, 121454. [[CrossRef](#)]
46. Li, J.H.; Kang, W.L.; Yang, X.; Yu, X.D.; Xu, L.L.; Guo, Y.H.; Fang, H.B.; Zhang, S.D. Mesoporous titania-based $\text{H}_3\text{PW}_{12}\text{O}_{40}$ composite by a block copolymer surfactant-assisted templating route: Preparation, characterization, and heterogeneous photocatalytic properties. *Desalination* **2010**, *255*, 107–116. [[CrossRef](#)]
47. Yang, C.D.; Feng, S.; Ma, C.C.; Zhou, Y.; Dai, X.J.; Ye, Z.W.; Wang, Y. $\text{Bi}_2\text{Sn}_2\text{O}_7/\text{UiO-66-NH}_2$ heterojunction photocatalyst simultaneously adsorbed and photodegraded tetracycline. *J. Environ. Chem. Eng.* **2023**, *11*, 109664. [[CrossRef](#)]

48. Wang, S.J.; Chen, L.; Zhao, X.L.; Zhang, J.Q.; Ao, Z.M.; Liu, W.R.; Wu, H.; Shi, L.; Yin, Y.; Xu, X.Y.; et al. Efficient photocatalytic overall water splitting on metal-free 1D SWCNT/2D ultrathin C_3N_4 heterojunctions via novel non-resonant plasmonic effect. *Appl. Catal. B-Environ.* **2020**, *278*, 119312. [CrossRef]
49. Li, S.Y.; Niu, Z.W.; Pan, D.Q.; Cui, Z.P.; Shang, H.W.; Lian, J.; Wu, W.S. Efficient photoreduction strategy for uranium immobilization based on graphite carbon nitride/activated carbon nanocomposites. *Chin. Chem. Lett.* **2022**, *33*, 3581–3584. [CrossRef]
50. Wu, C.; Dai, J.N.; Ma, J.; Zhang, T.Y.; Qiang, L.S.; Xue, J.Q. Mechanistic study of B-TiO₂/BiVO₄ S-scheme heterojunction photocatalyst for tetracycline hydrochloride removal and H₂ production. *Sep. Purif. Technol.* **2023**, *312*, 123398. [CrossRef]
51. Zhu, L.D.; Zhou, Y.X.; Fei, L.Y.; Cheng, X.L.; Zhu, X.X.; Deng, L.Q.; Ma, X. Z-scheme CuO/Fe₃O₄/GO heterojunction photocatalyst: Enhanced photocatalytic performance for elimination of tetracycline. *Chemosphere* **2022**, *309*, 136721. [CrossRef] [PubMed]
52. Wan, Y.; Wang, H.J.; Liu, J.J.; Liu, X.; Song, X.H.; Zhou, W.Q.; Zhang, J.S.; Huo, P.W. Enhanced degradation of polyethylene terephthalate plastics by CdS/CeO₂ heterojunction photocatalyst activated peroxy monosulfate. *J. Hazard. Mater.* **2023**, *452*, 131375. [CrossRef] [PubMed]
53. Santos, H.F.D.; Xavier, É.S.; Zerner, M.C.; Almeida, W.B.D. Spectroscopic investigation of the Al(III)-anhydrotetracycline complexation process. *J. Mol. Struct.* **2000**, *527*, 193–202. [CrossRef]
54. Yang, J.H.; Sun, J.L.; Chen, S.; Lan, D.Q.; Li, Z.H.; Li, Z.J.; Wei, J.W.; Yu, Z.B.; Zhu, H.X.; Wang, S.F.; et al. S-scheme 1 T phase MoSe₂/AgBr heterojunction toward antibiotic degradation: Photocatalytic mechanism, degradation pathways, and intermediates toxicity evaluation. *Sep. Purif. Technol.* **2022**, *290*, 120881. [CrossRef]
55. Gao, P.; Li, Z.X.; Feng, L.; Liu, Y.Z.; Du, Z.W.; Zhang, L.Q. Construction of novel MWCNTs/Bi₄O₅I₂ nanosheets with enhanced adsorption and photocatalytic performance for the degradation of tetracycline: Efficiency, mechanism and regeneration. *Chem. Eng. J.* **2022**, *429*, 132398. [CrossRef]
56. Abilarasu, A.; Kumar, P.S.; Vo, D.V.N.; Krithika, D.; Nguenagni, P.T.; Joshiba, G.J.; Carolin, C.F.; Prasannamedha, G. Enhanced photocatalytic degradation of diclofenac by Sn_{0.15}Mn_{0.85}Fe₂O₄ catalyst under solar light. *J. Environ. Chem. Eng.* **2021**, *9*, 104875. [CrossRef]
57. Shi, H.F.; Zhu, H.W.; Jin, T.; Chen, L.; Zhang, J.Y.; Qiao, K.Y.; Chen, Z. Construction of Bi/Polyoxometalate doped TiO₂ composite with efficient visible-light photocatalytic performance: Mechanism insight, degradation pathway and toxicity evaluation. *Appl. Surf. Sci.* **2023**, *615*, 156310. [CrossRef]
58. Chen, D.D.; Yi, X.H.; Zhao, C.; Fu, H.F.; Wang, P.; Wang, C.C. Polyaniline modified MIL-100(Fe) for enhanced photocatalytic Cr(VI) reduction and tetracycline degradation under white light. *Chemosphere* **2020**, *245*, 125659. [CrossRef]
59. Wang, H.X.; Liao, B.; Lu, T.; Ai, Y.L.; Liu, G. Enhanced visible-light photocatalytic degradation of tetracycline by a novel hollow BiOCl@CeO₂ heterostructured microspheres: Structural characterization and reaction mechanism. *J. Hazard. Mater.* **2020**, *385*, 12155. [CrossRef]
60. Chen, Z.; Gao, Y.T.; Chen, F.; Shi, H.F. Metallic NiSe cocatalyst decorated g-C₃N₄ with enhanced photocatalytic activity. *Chem. Eng. J.* **2023**, *413*, 127474. [CrossRef]
61. Liu, C.; He, X.X.; Xu, Q.X.; Chen, M. A general way to realize the bi-directional promotion effects on the photocatalytic removal of heavy metals and organic pollutants in real water by a novel S-scheme heterojunction: Experimental investigations, QSAR and DFT calculations. *J. Hazard. Mater.* **2023**, *445*, 130551. [CrossRef] [PubMed]
62. Liu, C.; Han, Z.T.; Feng, Y.; Dai, H.L.; Zhao, Y.F.; Han, N.; Zhang, Q.F.; Zou, Z.G. Ultrathin Z-scheme 2D/2D N-doped HTiNbO₅ nanosheets/g-C₃N₄ porous composites for efficient photocatalytic degradation and H₂ generation under visible light. *J. Colloid Interface Sci.* **2021**, *583*, 58–70. [CrossRef] [PubMed]
63. Shi, H.F.; Yan, G.; Zhang, Y.; Tan, H.Q.; Zhou, W.Z.; Ma, Y.Y.; Li, Y.G.; Chen, W.L.; Wang, E.B. Ag/Ag_xH_{3-x}PMo₁₂O₄₀ nanowires with enhanced visible light-driven photocatalytic performance. *ACS Appl. Mater. Interface* **2017**, *9*, 422–430. [CrossRef] [PubMed]
64. Chen, Z.; Gao, Y.T.; Mu, D.Z.; Shi, H.F.; Lou, D.W.; Liu, S.Y. Recyclable magnetic NiFe₂O₄/C yolk-shell nanospheres with excellent visible-light-Fenton degradation performance of tetracycline hydrochloride. *Dalton Trans.* **2019**, *48*, 3038–3044. [CrossRef] [PubMed]
65. Shi, H.F.; Tan, H.Q.; Zhu, W.B.; Sun, Z.C.; Ma, Y.J.; Wang, E.B. Electrospun Cr-doped Bi₄Ti₃O₁₂/Bi₂Ti₂O₇ heterostructure fibers with enhanced visible-light photocatalytic properties. *J. Mater. Chem. A* **2015**, *3*, 6586–6591. [CrossRef]
66. Wang, Y.H.; Han, D.M.; Wang, Z.H.; Gu, F.B. Efficient photocatalytic degradation of tetracycline under visible light by an all-solid-state Z-Scheme Ag₃PO₄/MIL-101(Cr) heterostructure with metallic Ag as a charge transmission bridge. *ACS Appl. Mater. Interface* **2023**, *15*, 22085–22100. [CrossRef] [PubMed]
67. Feng, S.; Xie, T.P.; Wang, J.K.; Yang, J.W.; Kong, D.S.; Liu, C.W.; Chen, S.L.; Yang, F.L.; Pan, M.J.; Yang, J.; et al. Photocatalytic activation of PMS over magnetic heterojunction photocatalyst SrTiO₃/BaFe₁₂O₁₉ for tetracycline ultrafast degradation. *Chem. Eng. J.* **2023**, *470*, 143900. [CrossRef]
68. Li, S.J.; Yan, R.Y.; Cai, M.J.; Jiang, W.; Zhang, M.Y.; Li, X. Enhanced antibiotic degradation performance of Cd_{0.5}Zn_{0.5}S/Bi₂MoO₆ S-scheme photocatalyst by carbon dot modification. *J. Mater. Sci. Technol.* **2023**, *164*, 59–67. [CrossRef]
69. Li, X.L.; Yang, G.Q.; Li, S.S.; Xiao, N.; Li, N.; Gao, Y.Q.; Lv, D.; Ge, L. Novel dual co-catalysts decorated Au@HCS@PdS hybrids with spatially separated charge carriers and enhanced photocatalytic hydrogen evolution activity. *Chem. Eng. J.* **2020**, *379*, 122350. [CrossRef]
70. Li, S.J.; Cai, M.J.; Wang, C.C.; Liu, Y.P. Ta₃N₅/CdS core-shell S-scheme heterojunction nanofibers for efficient photocatalytic removal of antibiotic tetracycline and Cr(VI): Performance and mechanism insights. *Adv. Fiber Mater.* **2023**, *5*, 994–1007. [CrossRef]

71. Li, S.J.; Wang, C.C.; Dong, K.X.; Zhang, P.; Chen, X.B.; Li, X. MIL-101(Fe)/BiOBr S-scheme photocatalyst for promoting photocatalytic abatement of Cr(VI) and enrofloxacin antibiotic: Performance and mechanism. *Chin. J. Catal.* **2023**, *51*, 101–112. [[CrossRef](#)]
72. Cai, Z.Q.; Song, Y.G.; Jin, X.B.; Wang, C.C.; Ji, H.D.; Liu, W.; Sun, X.B. Highly efficient AgBr/h-MoO₃ with charge separation tuning for photocatalytic degradation of trimethoprim: Mechanism insight and toxicity assessment. *Sci. Total. Environ.* **2021**, *781*, 146754. [[CrossRef](#)] [[PubMed](#)]
73. Fan, S.L.; Chen, J.; Tian, L.; Fan, C.; Xu, W.T.; Zhang, Y.J.; Gan, T.; Hu, H.Y.; Huang, Z.Q.; Qin, Y.B. Construction of a recyclable chitosan-based aerogel-supported TiO₂ catalyst for treating high-concentration surfactants. *Compos. Part. B-Eng.* **2023**, *251*, 110475. [[CrossRef](#)]
74. Zhou, Q.; Zhang, L.H.; Zhang, L.F.; Jiang, B.; Sun, Y.L. In-situ constructed 2D/2D ZnIn₂S₄/Bi₄Ti₃O₁₂ S-scheme heterojunction for degradation of tetracycline: Performance and mechanism insights. *J. Hazard. Mater.* **2022**, *438*, 129438. [[CrossRef](#)] [[PubMed](#)]
75. Liu, J.; Wang, H.; Li, W.J.; Xie, H.X.; Li, X.; Ge, B.; Yang, L.Q.; Chang, M.J.; Du, H.L.; Song, S.J. Controllable fabrication of Bi₄Ti₃O₁₂/C/Bi₂S₃/MoS₂ heterojunction with effective suppression of Bi₂S₃ assisted by amorphous carbon interlayer for significantly enhanced photocatalysis. *J. Taiwan Inst. Chem. E* **2023**, *146*, 104882. [[CrossRef](#)]
76. Shi, H.F.; Fu, J.C.; Jiang, W.; Wang, Y.T.; Liu, B.L.; Liu, J.X.; Ji, H.F.; Wang, W.D.; Chen, Z. Construction of g-C₃N₄/Bi₄Ti₃O₁₂ hollow nanofibers with highly efficient visible-light-driven photocatalytic performance. *Colloid Surf. A* **2021**, *615*, 126063. [[CrossRef](#)]
77. Sayed, M.; Yu, J.G.; Liu, G.; Jaroniec, M. Non-noble plasmonic metal-based photocatalysts. *Chem. Rev.* **2022**, *122*, 10484–10537. [[CrossRef](#)]
78. Jin, Z.Z.; Li, J.R.; Zhang, Y.M.; Liu, D.; Ding, H.; Mamba, B.B.; Kuvarega, A.T.; Gui, J.Z. Rational design of efficient visible-light photocatalysts (1D@2D/0D) ZnO@Ni-doped BiOBr/Bi heterojunction: Considerations on hierarchical structures, doping and SPR effect. *J. Mater. Sci. Technol.* **2022**, *125*, 38–50. [[CrossRef](#)]
79. He, D.; Chen, Y.; Situ, Y.; Zhong, L.; Huang, H. Synthesis of ternary g-C₃N₄/Ag/-FeOOH photocatalyst: An integrated heterogeneous fenton-like system for effectively degradation of azo dye methyl orange under visible light. *Appl. Surf. Sci.* **2017**, *425*, 862–872. [[CrossRef](#)]
80. Liang, J.X.; Hou, Y.P.; Zhu, H.X.; Xiong, J.H.; Huang, W.Y.; Yu, Z.B.; Wang, S.F. Levofloxacin degradation performance and mechanism in the novel electro-Fenton system constructed with vanadium oxide electrodes under neutral pH. *Chem. Eng. J.* **2021**, *433*, 133574. [[CrossRef](#)]
81. Gong, Y.N.; Wang, Y.; Tang, M.M.; Zhang, H.; Wu, P.; Liu, C.J.; He, J.; Jiang, W. A two-step process coupling photocatalysis with adsorption to treat tetracycline-Copper(II) hybrid wastewaters, degradation mechanism, pathways and biotoxicity evaluation. *J. Water. Process. Eng.* **2022**, *47*, 102710. [[CrossRef](#)]
82. Chen, L.J.; Li, Y.H.; Zhang, J.W.; Li, M.X.; Yin, W.Y.; Chen, X. Oxidative degradation of tetracycline hydrochloride by Mn₂O₃/Bi₂O₃ photocatalysis activated peroxy monosulfate. *Inorg. Chem. Commun.* **2022**, *140*, 109414. [[CrossRef](#)]
83. Zhang, X.M.; Wang, H.; Gao, M.M.; Zhao, P.F.; Xia, W.L.; Yang, R.L.; Huang, Y.C.; Wang, L.; Liu, M.X.; Wei, T.; et al. Template-directed synthesis of pomegranate-shaped zinc oxide@zeolitic imidazolate framework for visible light photocatalytic degradation of tetracycline. *Chemosphere* **2022**, *294*, 133782. [[CrossRef](#)] [[PubMed](#)]
84. Yin, W.Q.; Cao, X.J.; Wang, B.; Jiang, Q.; Chen, Z.G.; Xia, J.X. In-situ synthesis of MoS₂/BiOBr material via mechanical ball milling for boosted photocatalytic degradation pollutants performance. *ChemistrySelect* **2021**, *6*, 928–936. [[CrossRef](#)]
85. Wu, S.Q.; Li, X.Y.; Tian, Y.Q.; Lin, Y.; Hu, Y.H. Excellent photocatalytic degradation of tetracycline over black anatase-TiO₂ under visible light. *Chem. Eng. J.* **2021**, *406*, 126747. [[CrossRef](#)]
86. Li, S.Y.; Tang, Y.W.; Wang, M.; Kang, J.; Jin, C.Y.; Liu, J.Y.; Li, Z.L.; Zhu, J.W. NiO/g-C₃N₄ 2D/2D heterojunction catalyst as efficient peroxy monosulfate activators toward tetracycline degradation: Characterization, performance and mechanism. *J. Alloys Compd.* **2021**, *880*, 160547. [[CrossRef](#)]
87. Shen, X.F.; Zhang, Y.; Shi, Z.; Shan, S.D.; Liu, J.S.; Zhang, L.S. Construction of C₃N₄/CdS nanojunctions on carbon fiber cloth as a filter-membrane-shaped photocatalyst for degrading flowing wastewater. *J. Alloys Compd.* **2021**, *851*, 156743. [[CrossRef](#)]
88. Ghoreishian, S.M.; Ranjith, K.S.; Lee, H.; Park, B.; Norouzi, M.; Nikoo, S.Z.; Kim, W.S.; Han, Y.K.; Huh, Y.S. Tuning the phase composition of 1D TiO₂ by Fe/Sn co-doping strategy for enhanced visible-light-driven photocatalytic and photoelectrochemical performances. *J. Alloys Compd.* **2021**, *851*, 156826. [[CrossRef](#)]
89. Jiang, H.; Wang, Q.; Chen, P.; Zheng, H.; Shi, J.; Shu, H.; Liu, Y. Photocatalytic degradation of tetracycline by using a regenerable (Bi)BiOBr/rGO composite. *J. Clean. Prod.* **2022**, *339*, 130771. [[CrossRef](#)]
90. Chen, Z.J.; Guo, H.; Liu, H.Y.; Niu, C.G.; Huang, D.W.; Yang, Y.Y.; Liang, C.; Li, L.; Li, J.C. Construction of dual S-scheme Ag₂CO₃/Bi₄O₅I₂/g-C₃N₄ heterostructure photocatalyst with enhanced visible-light photocatalytic degradation for tetracycline. *Chem. Eng. J.* **2022**, *438*, 135471. [[CrossRef](#)]
91. Cestaro, R.; Philippe, L.; Serrà, A.; Gómez, E.; Schmutz, P. Electrodeposited manganese oxides as efficient photocatalyst for the degradation of tetracycline antibiotics pollutant. *Chem. Eng. J.* **2023**, *462*, 142202. [[CrossRef](#)]
92. Mahmoodi, M.; Rafiee, E.; Eavani, S. Photocatalytic removal of toxic dyes, liquorice and tetracycline wastewaters by a mesoporous photocatalyst under irradiation of different lamps and sunlight. *J. Environ. Manag.* **2022**, *313*, 115023. [[CrossRef](#)] [[PubMed](#)]
93. Chen, Z.G.; Chen, X.L.; Di, J.; Liu, Y.L.; Yin, S.; Xia, J.X.; Li, H.M. Graphene-like boron nitride modified bismuth phosphate materials for boosting photocatalytic degradation of enrofloxacin. *J. Colloid Interface Sci.* **2017**, *492*, 51–60. [[CrossRef](#)] [[PubMed](#)]

94. Liu, Y.C.; Li, G.B.; Wang, D.; Zhong, Z.C.; Hu, K.B.; Zhang, C.Q.; Hu, G.P.; Li, X.W.; Wan, Y.H. Lanthanide-doped upconversion glass-ceramic photocatalyst fabricated from fluorine-containing waste for the degradation of organic pollutants. *J. Colloid Interface Sci.* **2023**, *638*, 461–473. [[CrossRef](#)]
95. Huang, J.X.; Li, D.G.; Li, R.B.; Chen, P.; Zhang, Q.X.; Liu, H.J.; Lv, W.Y.; Liu, G.G.; Feng, Y.P. One-step synthesis of phosphorus/oxygen co-doped g-C₃N₄/anatase TiO₂ Z-scheme photocatalyst for significantly enhanced visible-light photocatalysis degradation of enrofloxacin. *J. Hazard. Mater.* **2020**, *386*, 12. [[CrossRef](#)]
96. Wen, X.J.; Niu, C.G.; Zhang, L.; Liang, C.; Zeng, G.M. A novel Ag₂O/CeO₂ heterojunction photocatalysts for photocatalytic degradation of enrofloxacin: Possible degradation pathways; mineralization activity and an in depth mechanism insight. *Appl. Catal. B-Environ.* **2018**, *221*, 701–714. [[CrossRef](#)]
97. Cai, M.J.; Liu, Y.P.; Wang, C.C.; Lin, W.; Li, S.J. Novel Cd_{0.5}Zn_{0.5}S/Bi₂MoO₆ S-scheme heterojunction for boosting the photodegradation of antibiotic enrofloxacin: Degradation pathway; mechanism and toxicity assessment. *Sep. Purif. Technol.* **2023**, *304*, 11. [[CrossRef](#)]
98. Li, T.C.; Liu, J.X.; Shi, F.; Zhang, H.Y.; Zhang, H.J.; Ma, C.C.; Wasim, M. A novel S-type Cs_xWO₃/BiOI heterojunction photocatalyst constructed in graphene aerogel with high degradation efficiency for enrofloxacin: Degradation mechanism and DFT calculation. *J. Environ. Chem. Eng.* **2023**, *11*, 109301. [[CrossRef](#)]
99. Xiao, L.Q.; Zhang, S.Y.; Chen, B.Q.; Wu, P.P.; Feng, N.D.; Deng, F.; Wang, Z. Visible-light photocatalysis degradation of enrofloxacin by crawfish shell biochar combined with g-C₃N₄: Effects and mechanisms. *J. Environ. Chem. Eng.* **2023**, *11*, 109693. [[CrossRef](#)]
100. Huang, P.Q.; Luan, J.F. Synthesis of a GaOOH/ZnBiTaO₅ heterojunction photocatalyst with enhanced photocatalytic performance toward enrofloxacin. *RSC Adv.* **2020**, *10*, 4286–4292. [[CrossRef](#)]
101. Sciscenko, I.; Mestre, S.; Climent, J.; Valero, F.; Escudero-Onate, C.; Oller, I.; Arques, A. Magnetic Photocatalyst for Wastewater Tertiary Treatment at Pilot Plant Scale: Disinfection and Enrofloxacin Abatement. *Water* **2021**, *13*, 12. [[CrossRef](#)]
102. Su, Y.H.; Chen, P.; Wang, F.L.; Zhang, Q.X.; Chen, T.S.; Wang, Y.F.; Yao, K.; Lv, W.Y.; Liu, G.G. Decoration of TiO₂/g-C₃N₄ Z-scheme by carbon dots as a novel photocatalyst with improved visible-light photocatalytic performance for the degradation of enrofloxacin. *RSC Adv.* **2017**, *7*, 34096–34103. [[CrossRef](#)]
103. Huang, P.Q.; Luan, J.F. Dispersed GaOOH rods loaded on the surface of ZnBiNbO₅ particles with enhanced photocatalytic activity toward enrofloxacin. *RSC Adv.* **2019**, *9*, 32027–32033. [[CrossRef](#)]
104. Yu, Y.Q.; Yan, L.; Cheng, J.M.; Jing, C.Y. Mechanistic insights into TiO₂ thickness in Fe₃O₄@TiO₂-GO composites for enrofloxacin photodegradation. *Chem. Eng. J.* **2017**, *325*, 647–654. [[CrossRef](#)]
105. Mahjoub, A.R.; Rahmani, H.; Khazaei, Z. Bimetallic CuAg alloyed nanoparticles anchored on CdS nanorods for the photocatalytic degradation of enrofloxacin. *ACS Appl. Nano. Mater.* **2023**, *6*, 4554–4566.
106. Luan, J.F.; Liu, W.L.; Yao, Y.; Ma, B.B.; Niu, B.W.; Yang, G.M.; Wei, Z.J. Synthesis and Property Examination of Er₂FeSbO₇/BiTiSbO₆ Heterojunction Composite Catalyst and Light-Catalyzed Retrogradation of Enrofloxacin in Pharmaceutical Waste Water under Visible Light Irradiation. *Materials* **2022**, *15*, 26. [[CrossRef](#)] [[PubMed](#)]
107. Zhao, Y.J.; Liu, X.T.; Gu, S.N.; Liu, J.M. Enhanced photocatalytic performance of rhodamine B and enrofloxacin by Pt loaded Bi₄V₂O₁₁: Boosted separation of charge carriers; additional superoxide radical production; and the photocatalytic mechanism. *RSC Adv.* **2021**, *11*, 9746–9755. [[CrossRef](#)] [[PubMed](#)]
108. Tian, J.L.; Wu, S.; Liu, S.X.; Zhang, W. Photothermal enhancement of highly efficient photocatalysis with bioinspired thermal radiation balance characteristics. *Appl. Surf. Sci.* **2022**, *592*, 153304. [[CrossRef](#)]
109. Sane, P.K.; Rakte, D.; Tambat, S.; Bhalinge, R.; Sontakke, S.M.; Nemade, P. Enhancing solar photocatalytic activity of Bi₅O₇I photocatalyst with activated carbon heterojunction. *Adv. Powder. Technol.* **2022**, *33*, 103357. [[CrossRef](#)]
110. Harikumar, B.; Okla, M.K.; Alaraidh, I.A.; Mohebaldi, A.; Soufa, W.; Abdel-Maksoud, M.A.; Aufy, M.; Thomas, A.M.; Raju, L.L.; Khan, S. Robust visible light active CoNiO₂-BiFeO₃-NiS ternary nanocomposite for photo-fenton degradation of rhodamine B and methyl orange: Kinetics; degradation pathway and toxicity assessment. *J. Environ. Manag.* **2022**, *317*, 115321. [[CrossRef](#)] [[PubMed](#)]
111. Bi, H.F.; Liu, J.S.; Wu, Z.Y.; Zhu, K.J.; Suo, H.; Lv, X.L.; Fu, Y.L.; Jian, R.; Sun, Z.B. Construction of Bi₂WO₆/ZnIn₂S₄ with Z-scheme structure for efficient photocatalytic performance. *Chem. Phys. Lett.* **2021**, *769*, 138449. [[CrossRef](#)]
112. Van, N.U.; Thuy, N.P.; Hanh, V.N.; Loan, D.T.; Vuong, D.B.; Thao, T.T. Low-temperature designing of BiVO₄ nanocubes with coexposed {010}/{110} facets for solar light photocatalytic degradation of methyl orange and diazinon. *Inorg. Chem. Commun.* **2022**, *136*, 109136. [[CrossRef](#)]
113. Hieu, V.Q.; Phung, T.K.; Nguyen, T.; Khan, A.; Doan, V.D.; Tran, V.A.; Le, V.T. Photocatalytic degradation of methyl orange dye by Ti₃C₂-eTiO₂ heterojunction under solar light. *Chemosphere* **2021**, *276*, 130154. [[CrossRef](#)] [[PubMed](#)]
114. Wang, L.; Li, T.; Tao, L.L.; Lei, H.W.; Ma, P.Y.; Liu, J. A novel copper-doped porous carbon nanospheres film prepared by onestep ultrasonic spray pyrolytic of sugar for photocatalytic degradation of methyl orange. *Process. Saf. Environ.* **2022**, *158*, 79–86. [[CrossRef](#)]
115. Menon, S.G.; Bedyala, A.K.; Pathak, T.; Kumara, V.; Swart, H.C. Sr₄Al₁₄O₂₅: Eu²⁺, Dy³⁺@ZnO nanocomposites as highly efficient visible light photocatalysts for the degradation of aqueous methyl orange. *J. Alloys Compd.* **2021**, *860*, 158370. [[CrossRef](#)]
116. Li, J.W.; He, M.Z.; Yan, J.K.; Liu, J.H.; Zhang, J.X.; Ma, J.J. Room temperature engineering crystal facet of Cu₂O for photocatalytic degradation of methyl orange. *Nanomaterials* **2022**, *10*, 1697. [[CrossRef](#)]

117. Kanakaraju, D.; Jasni, M.A.A.; Lim, Y.C. A highly photoresponsive and efficient molybdenum modified titanium dioxide photocatalyst for the degradation of methyl orange. *Int. J. Environ. Sci. Technol.* **2022**, *19*, 5579–5594. [[CrossRef](#)]
118. Lu, G.F.; Liu, X.D.; Zhang, P.; Xu, S.T.; Gao, Y.J.; Yu, S.Y. Preparation and Photocatalytic Studies on Nanocomposites of 4-Hydroxyphenyl-Substituted Corrole/TiO₂ towards Methyl Orange Photodegradation. *ChemistrySelect* **2021**, *6*, 6841–6846. [[CrossRef](#)]
119. Kourab, P.; Mukherjee, S.P. CsPbBr₃/Cs₄PbBr₆ perovskite@COF nanocomposites for visible-light-driven photocatalytic applications in water. *J. Mater. Chem. A* **2021**, *9*, 6819–6826.
120. Arumugam, M.; Seralathan, K.; Praserthdam, S.; Tahir, M.P. Synthesis of novel graphene aerogel encapsulated bismuth oxyiodide composite towards effective removal of methyl orange azo-dye under visible light. *Chemosphere* **2022**, *303*, 135121. [[CrossRef](#)]
121. Tang, H.D.; Zhang, W.J.; Meng, Y.; Xie, B.; Ni, Z.M.; Xia, S.J. Investigation onto the performance and mechanism of visible light photodegradation of methyl orange catalyzed by M/CeO₂ (M = Pt; Ag; Au). *Mater. Res. Bull.* **2021**, *144*, 111497. [[CrossRef](#)]
122. Aadnan, I.; Zegaoui, O.; Mragui, A.E.; Silva, J.C.G.E. Physicochemical and photocatalytic properties under visible light of ZnO-Bentonite/Chitosan hybrid-biocomposite for water remediation. *Nanomaterials* **2022**, *12*, 102. [[CrossRef](#)] [[PubMed](#)]

Disclaimer/Publisher's Note: The statements, opinions and data contained in all publications are solely those of the individual author(s) and contributor(s) and not of MDPI and/or the editor(s). MDPI and/or the editor(s) disclaim responsibility for any injury to people or property resulting from any ideas, methods, instructions or products referred to in the content.